

U.S.N.A. --- Trident Scholar project report; no. 333 (2005)

**EFFECTS OF PULSING ON FILM COOLING
OF GAS TURBINE AIRFOILS**

by

Midshipman 1/c Sarah M. Coulthard, Class of 2005
United States Naval Academy
Annapolis, Maryland

(signature)

Certification of Advisers Approval

Associate Professor Ralph J. Volino
Mechanical Engineering Department

(signature)

(date)

Professor Karen A. Flack
Mechanical Engineering Department

(signature)

(date)

Acceptance for the Trident Scholar Committee

Professor Joyce E. Shade
Deputy Director of Research & Scholarship

(signature)

(date)

REPORT DOCUMENTATION PAGE			Form Approved OMB No. 074-0188	
Public reporting burden for this collection of information is estimated to average 1 hour per response, including g the time for reviewing instructions, searching existing data sources, gathering and maintaining the data needed, and completing and reviewing the collection of information. Send comments regarding this burden estimate or any other aspect of the collection of information, including suggestions for reducing this burden to Washington Headquarters Services, Directorate for Information Operations and Reports, 1215 Jefferson Davis Highway, Suite 1204, Arlington, VA 22202-4302, and to the Office of Management and Budget, Paperwork Reduction Project (0704-0188), Washington, DC 20503.				
1. AGENCY USE ONLY (Leave blank)		2. REPORT DATE 9 May 2005		3. REPORT TYPE AND DATE COVERED
4. TITLE AND SUBTITLE Effects of pulsing on film cooling of gas turbine airfoils			5. FUNDING NUMBERS	
6. AUTHOR(S) Coulthard, Sarah M. (Sarah Marie), 1983-				
7. PERFORMING ORGANIZATION NAME(S) AND ADDRESS(ES)			8. PERFORMING ORGANIZATION REPORT NUMBER	
9. SPONSORING/MONITORING AGENCY NAME(S) AND ADDRESS(ES)			10. SPONSORING/MONITORING AGENCY REPORT NUMBER	
US Naval Academy Annapolis, MD 21402			Trident Scholar project report no. 333 (2005)	
11. SUPPLEMENTARY NOTES				
12a. DISTRIBUTION/AVAILABILITY STATEMENT This document has been approved for public release; its distribution is UNLIMITED.				12b. DISTRIBUTION CODE
13. ABSTRACT: The objective of this project was to determine the effects of pulsed film cooling on turbine blades. High combustor temperatures, resulting in elevated turbine inlet temperatures, produce high engine efficiency. At current operating temperatures, the turbine inlet temperature is above the melting point of the turbine blades. Thus cooling the blades in the first stages after the combustor is essential. Current methods for film cooling utilize a continuous stream of bleed air from the compressor. This air is routed into a cavity inside each blade and bled out of holes onto the blade surface, creating a film of cool air. Pulsed film cooling may reduce the amount of bleed air used, thus increasing the efficiency of the engine by allowing more air to flow through the combustor, while providing equivalent protection for the blades. In this study, a section of a turbine blade was modeled using a plate with a row of five film cooling holes. Coolant air was pulsed via solenoid valves from a plenum, while a wind tunnel provided a mainstream flow. Temperature and velocity fields were measured over the blade surface with varying blowing rates of the coolant and frequencies of pulsing. The film cooling effectiveness, a measure of how well the coolant protects the blade surface, was calculated based on the measured temperatures. The results were compared to baseline cases with continuous blowing and no blowing. The overall best case was continuous film cooling with the jet velocity one fourth of the mainstream velocity. However, results showed that pulsed film cooling has the potential to provide an equivalent or greater film cooling effectiveness for higher jet velocities. The case of pulsed jets with a jet velocity equal to the mainstream velocity, pulsing frequency of 20 Hertz, and 75% duty cycle showed an increased film cooling effectiveness and decreased heat transfer compared to the continuous blowing case. This study suggests that pulsed film cooling has the potential to adequately protect gas turbine blades with additional research, ultimately allowing for an increased efficiency in a gas turbine engine.				
14. SUBJECT TERMS: Turbine blade ; Film cooling ; Pulsed jet			15. NUMBER OF PAGES 70	
			16. PRICE CODE	
17. SECURITY CLASSIFICATION OF REPORT	18. SECURITY CLASSIFICATION OF THIS PAGE	19. SECURITY CLASSIFICATION OF ABSTRACT	20. LIMITATION OF ABSTRACT	

ABSTRACT: The objective of this project was to determine the effects of pulsed film cooling on turbine blades. High combustor temperatures, resulting in elevated turbine inlet temperatures, produce high engine efficiency. At current operating temperatures, the turbine inlet temperature is above the melting point of the turbine blades. Thus cooling the blades in the first stages after the combustor is essential. Current methods for film cooling utilize a continuous stream of bleed air from the compressor. This air is routed into a cavity inside each blade and bled out of holes onto the blade surface, creating a film of cool air. Pulsed film cooling may reduce the amount of bleed air used, thus increasing the efficiency of the engine by allowing more air to flow through the combustor, while providing equivalent protection for the blades. In this study, a section of a turbine blade was modeled using a plate with a row of five film cooling holes. Coolant air was pulsed via solenoid valves from a plenum, while a wind tunnel provided a mainstream flow. Temperature and velocity fields were measured over the blade surface with varying blowing rates of the coolant and frequencies of pulsing. The film cooling effectiveness, a measure of how well the coolant protects the blade surface, was calculated based on the measured temperatures. The results were compared to baseline cases with continuous blowing and no blowing. The overall best case was continuous film cooling with the jet velocity one fourth of the mainstream velocity. However, results showed that pulsed film cooling has the potential to provide an equivalent or greater film cooling effectiveness for higher jet velocities. The case of pulsed jets with a jet velocity equal to the mainstream velocity, pulsing frequency of 20 Hertz, and 75% duty cycle showed an increased film cooling effectiveness and decreased heat transfer compared to the continuous blowing case. This study suggests that pulsed film cooling has the potential to adequately protect gas turbine blades with additional research, ultimately allowing for an increased efficiency in a gas turbine engine.

Keywords

Turbine blade

Film cooling

Pulsed jet

Acknowledgments

I would like to thank Professor Volino and Professor Flack for their everlasting help with this project. They have taught me how to research, develop, and complete a project of this caliber. I have learned many important lessons from them and without their help this project would have been impossible. I would also like to thank the Machine Shop, Woodworking Shop, Fluids Laboratory, and Aerospace Laboratory for their assistance and support. Finally, I would like to thank Professor Shade and the Trident Scholar Committee for their continual dedication.

Table of Contents

Abstract.....	1
Keywords.....	2
Acknowledgements.....	3
List of Figures.....	5
List of Equations.....	8
Nomenclature.....	9
Introduction.....	10
Background.....	14
Modeling.....	18
Reynolds Number.....	19
Prandtl Number.....	19
Blowing Ratio.....	20
Mach Number.....	20
Film Cooling Effectiveness.....	21
Stanton Number.....	21
Convective Heat Flux.....	22
Heat Flux Ratio.....	23
Experimental Facilities.....	24
Wind Tunnel.....	24
Test Plate.....	26
Film Cooling Supply Plenum	28
Instrumentation.....	29
Thermocouples.....	30
Hot Wire.....	31
Cold Wire	32
Infrared Camera.....	33
Uncertainty.....	35
Results.....	35
Baseline Results – No Film Cooling.....	36
Continuous Film Cooling Results – Film Cooling Effectiveness.....	37
Continuous Film Cooling Results – Stanton Number.....	42
Pulsed Film Cooling Results.....	46
Pulsed Film Cooling Results – Varying Frequency.....	46
Pulsed Film Cooling Results – Varying Duty Cycle.....	55
Conclusions.....	60
Bibliography.....	61
Appendix A – Details of the Unheated Starting Length.....	64

List of Figures

Figure 1: Schematic of a standard turbine engine for aircraft propulsion.....	11
Figure 2: Thermodynamic cycle of a general turbine engine.	11
Figure 3: Turbine blade with cooling holes.	13
Figure 4: Series of rotating turbine blades.	13
Figure 5: Wind tunnel.....	25
Figure 6: Blower.	25
Figure 7: AC variable frequency driver.	25
Figure 8: Diffuser.	26
Figure 9: Heat exchanger and settling chamber.	26
Figure 10: Nozzle.	26
Figure 11: Nozzle connecting to test plate.	26
Figure 12: Wall opposite the starting length and side walls.....	28
Figure 13: Heater configuration.....	28
Figure 14: Film cooling holes.	28
Figure 15: Film cooling tank supply plenum.	29
Figure 16: Solenoid valves.	29
Figure 17: Single solenoid valve.	30
Figure 18: All cooling tank equipment.	30
Figure 19: Measuring devices.	30
Figure 20: Single thermocouple.	31
Figure 21: Thermocouple distribution on test plate.	31
Figure 22: Hot wire.....	33
Figure 23: Cold wire.....	33
Figure 24: Probe holder.....	33
Figure 25: Three axes traverse.....	33
Figure 26: IR camera.	34
Figure 27: Image to show camera sensitivity.....	34
Figure 28: Temperature profile of center hole at $B=0.5$	35
Figure 29: Velocity profile of center hole at $B=0.5$	35
Figure 30: Film cooling effectiveness contour plot for $B=0.125$ continuous.....	38
Figure 31: Centerline film cooling effectiveness for $B=0.125$ continuous.....	38
Figure 32: Film cooling effectiveness contour plot for $B=0.25$ continuous.....	38
Figure 33: Centerline film cooling effectiveness for $B=0.25$ continuous.....	38
Figure 34: Film cooling effectiveness contour plot for $B=0.5$ continuous.....	39
Figure 35: Centerline film cooling effectiveness for $B=0.5$ continuous.....	39
Figure 36: Film cooling effectiveness contour plot for $B=1.0$ continuous.....	39
Figure 37: Centerline film cooling effectiveness for $B=1.0$ continuous.....	39
Figure 38: Film cooling effectiveness contour plot for $B=1.5$ continuous.....	40
Figure 39: Centerline film cooling effectiveness for $B=1.5$ continuous.....	40
Figure 40: Cold wire temperature planes.....	41
Figure 41: $B=0.25$ at $x=3.5D$	41
Figure 42: $B=0.25$ at $x=7D$	41
Figure 43: $B=0.25$ at $x=14D$	41

Figure 44: $B=0.5$ at $x=3.5D$	41
Figure 45: $B=0.5$ at $x=7D$	41
Figure 46: $B=0.5$ at $x=14D$	41
Figure 47: $B=1.0$ at $x=3.5D$	41
Figure 48: $B=1.0$ at $x=7D$	41
Figure 49: $B=1.0$ at $x=14D$	41
Figure 50: $B=1.5$ at $x=3.5D$	42
Figure 51: $B=1.5$ at $x=7D$	42
Figure 52: $B=1.5$ at $x=14D$	42
Figure 53: Centerline film cooling effectiveness.....	42
Figure 54: Spanwise average film cooling effectiveness.....	42
Figure 55: St_f/St_o at $B=0.25$ with unheated starting length.....	44
Figure 56: St_f/St_o at $B=0.25$ with heated starting length.....	44
Figure 57: St_f/St_o at $B=0.5$ with unheated starting length.....	44
Figure 58: St_f/St_o at $B=0.5$ with heated starting length.....	44
Figure 59: St_f/St_o at $B=1.0$ with unheated starting length.....	45
Figure 60: St_f/St_o at $B=1.0$ with heated starting length.....	45
Figure 61: St_f/St_o at $B=1.5$ with unheated starting length.....	45
Figure 62: St_f/St_o at $B=1.5$ with heated starting length.....	45
Figure 63: Film cooling effectiveness contour plot for $F=10$ $DC=0.5$ $B=0.25$	49
Figure 64: Film cooling effectiveness contour plot for $F=20$ $DC=0.5$ $B=0.25$	49
Figure 65: Centerline film cooling effectiveness plot for $B=0.25$	49
Figure 66: Centerline Stanton number ratio plot for $B=0.25$	49
Figure 67: Centerline heat flux ratio plot for $B=0.25$	49
Figure 68: Film cooling effectiveness contour plot for $F=10$ $DC=0.5$ $B=0.5$	50
Figure 69: Film cooling effectiveness contour plot for $F=20$ $DC=0.5$ $B=0.5$	50
Figure 70: Centerline film cooling effectiveness plot for $B=0.5$	50
Figure 71: Centerline Stanton number ratio plot for $B=0.5$	50
Figure 72: Centerline heat flux ratio plot for $B=0.5$	50
Figure 73: Four frames of 24 frame cycle to show temperature profile for $F=10$ $DC=0.5$ $B=0.5$ at $x=3.5D$	50
Figure 74: Four frames of 24 frame cycle to show temperature profile for $F=20$ $DC=0.5$ $B=0.5$ at $x=3.5D$	51
Figure 75: Film cooling effectiveness contour plot for $F=10$ $DC=0.5$ $B=1.0$	53
Figure 76: Film cooling effectiveness contour plot for $F=20$ $DC=0.5$ $B=1.0$	53
Figure 77: Centerline film cooling effectiveness plot for $B=1.0$	53
Figure 78: Centerline Stanton number ratio plot for $B=1.0$	53
Figure 79: Centerline heat flux ratio plot for $B=1.0$	53
Figure 80: Film cooling effectiveness contour plot for $F=10$ $DC=0.5$ $B=1.5$	54
Figure 81: Film cooling effectiveness contour plot for $F=20$ $DC=0.5$ $B=1.5$	54
Figure 82: Centerline film cooling effectiveness plot for $B=1.5$	54
Figure 83: Centerline Stanton number ratio plot for $B=1.5$	54
Figure 84: Centerline heat flux ratio plot for $B=1.5$	54
Figure 85: Four frames of 24 frame cycle to show temperature profile for $F=10$ $DC=0.5$ $B=1.0$ at $x=3.5D$	54

Figure 86: Four frames of 24 frame cycle to show temperature profile for F=20 DC=0.5 B=1.0 at x=3.5D.....	55
Figure 87: Film cooling effectiveness contour plot for F=20 DC=0.25 B=0.5.....	57
Figure 88: Film cooling effectiveness contour plot for F=20 DC=0.75 B=0.5.....	57
Figure 89: Centerline film cooling effectiveness plot for B=0.5 with varying duty cycle...	57
Figure 90: Centerline Stanton number ratio plot for B=0.5 with varying duty cycle.....	57
Figure 91: Centerline heat flux ratio plot for B=0.5 with varying duty cycle.....	57
Figure 92: Film cooling effectiveness contour plot for F=20 DC=0.25 B=1.0.....	58
Figure 93: Film cooling effectiveness contour plot for F=20 DC=0.75 B=1.0.....	58
Figure 94: Centerline film cooling effectiveness plot for B=1.0 with varying duty cycle...	58
Figure 95: Centerline Stanton number ratio plot for B=1.0 with varying duty cycle.....	58
Figure 96: Centerline heat flux ratio plot for B=1.0 with varying duty cycle.....	58
Figure 97: Four frames of 24 frame cycle to show temperature profile for F=20 DC=0.25 B=0.5 at x=3.5D.....	58
Figure 98: Four frames of 24 frame cycle to show temperature profile for F=20 DC=0.75 B=0.5 at x=3.5D.....	59
Figure 99: Four frames of 24 frame cycle to show temperature profile for F=20 DC=0.25 B=1.0 at x=3.5D.....	59
Figure 100: Four frames of 24 frame cycle to show temperature profile for F=20 DC=0.75 B=1.0 at x=3.5D.....	59
Figure A-1: St_f/St_o at B=0.25 and x/D=1.....	65
Figure A-2: St_f/St_o at B=0.25 and x/D=6.....	65
Figure A-3: St_f/St_o at B=0.25 and x/D=12.....	65
Figure A-4: St_f/St_o at B=0.5 and x/D=1.....	65
Figure A-5: St_f/St_o at B=0.5 and x/D=6.....	65
Figure A-6: St_f/St_o at B=0.5 and x/D=12.....	65
Figure A-7: St_f/St_o at B=1.0 and x/D=1.....	66
Figure A-8: St_f/St_o at B=1.0 and x/D=6.....	66
Figure A-9: St_f/St_o at B=1.0 and x/D=12.....	66
Figure A-10: St_f/St_o at B=1.5 and x/D=1.....	66
Figure A-11: St_f/St_o at B=1.5 and x/D=6.....	66
Figure A-12: St_f/St_o at B=1.5 and x/D=12.....	66
Figure A-13: Temperature variation for B=0.5 at x/D=3.5.....	68
Figure A-14: Temperature variation for B=0.5 at x/D=7.....	68
Figure A-15: Temperature variation for B=0.5 at x/D=14.....	68
Figure A-16: Temperature variation for B=1.0 at x/D=3.5.....	68
Figure A-17: Temperature variation for B=1.0 at x/D=7.....	69
Figure A-18: Temperature variation for B=1.0 at x/D=14.....	69
Table 1: Test matrix.....	36
Table 2: Results.....	60

List of Equations

Equation 1: Pressure ratio for an ideal gas.....	12
Equation 2: Pressure ratio for an ideal compressor.....	12
Equation 3: Thermal efficiency of an engine.....	12
Equation 4: Power per unit mass of an engine.....	12
Equation 5: Thermal efficiency of an engine.....	12
Equation 6: Power per unit mass of an engine.....	13
Equation 7: Reynolds number.....	19
Equation 8: Prandtl number.....	19
Equation 9: Blowing ratio.....	20
Equation 10: Mach number.....	20
Equation 11: Film cooling effectiveness.....	21
Equation 12: Stanton number.....	21
Equation 13: Convective heat flux.....	22
Equation 14: Heat flux ratio.....	23
Equation 15: Jet velocity.....	29
Equation 16: Hot wire calibration.....	32
Equation 17: Cold wire calibration.....	32
Equation 18: Frequency.....	46
Equation 19: Duty cycle.....	46

Nomenclature

B	Blowing ratio – ratio of film cooling jet velocity to freestream velocity.
c	Speed of sound.
C_f	Skin friction coefficient.
C_p	Specific heat at constant pressure.
D	Film cooling hole diameter.
FSTI	Freestream turbulence intensity.
h	Heat transfer coefficient.
k	Specific heat ratio for a gas (used for engine efficiency and power output).
k	Thermal conductivity (used for conduction).
L	Length of the film cooling delivery tube.
L/D	Ratio of length to diameter of the film cooling hole.
M	Mach number.
P	Pressure.
Pr	Prandtl number.
q''	Heat flux.
Re_D	Reynolds number based on film cooling hole diameter.
Re_θ	Reynolds number based on boundary layer thickness.
r_p	Pressure ratio, P_2/P_1
St	Stanton number.
t	Plate thickness.
T	Temperature.
V	Velocity.
x	Streamwise distance from the downstream edge of the film cooling hole.
y	Normal distance from the test plate.
z	Spanwise distance from the center of the middle film cooling hole.

Greek Nomenclature

α	Thermal diffusivity.
ε	Emissivity.
η	Film cooling effectiveness.
η_{th}	Engine thermal efficiency.
ν	Kinematic viscosity of the flow.
σ	Stefan-Boltzmann constant.

Subscripts

1	Compressor inlet.	2	Combustor inlet.
3	Turbine inlet.	4	Turbine exhaust.
back	Back of test plate.	cond	Conduction.
conv	Convection.	f	With film cooling.
o	Without film cooling.	rad	Radiation.
surr	Surroundings, wall of laboratory.	wall	Plate surface condition.
∞	Mainstream flow.		

Introduction

Gas turbines are vital instruments in the technological world, providing the primary means for powering machinery ranging from generators to power plants; from ships to aircraft. Ways to increase the efficiency of these turbines are constantly being explored in order to reduce fuel consumption and cost, and increase mission lengths and power. One new technique under consideration in the present investigation is pulsing the film cooling jets on the turbine blades.

A gas turbine engine, as shown in Figure 1 (Pratt and Whitney, 2002), is comprised of three main components: a compressor, a combustion chamber, and a turbine. Atmospheric air first enters through a fan into a compressor, where it travels through a series of rotating blades and stationary vanes, causing the pressure and temperature to increase. The air then flows into the combustion chamber where it mixes with a sprayed fuel, and the mixture is ignited, causing combustion. This process creates a high temperature, high pressure, and high velocity flow that drives the turbine blades. The flow causes the blades to rotate, as the gas expands and the pressure drops. A representation of this process is depicted in Figure 2 (Çengel and Boles, 2002). The turbine blades are attached to a shaft which transfers the rotation of the blades into functional work. A portion of the work produced by the expansion process is needed to drive the compressor; the rest is used for the actual application. The two most common uses of the work involve power generation and aircraft propulsion. Power turbines need to produce shaft rotation in order to drive other machinery; therefore these turbines allow the gas to expand completely back to atmospheric pressure to produce the maximum power possible. Aircraft engine turbines, in contrast, first expand the gas to the amount required to power the compressor and fan. The gas is then expanded through an attached nozzle in order to provide thrust to propel the aircraft.

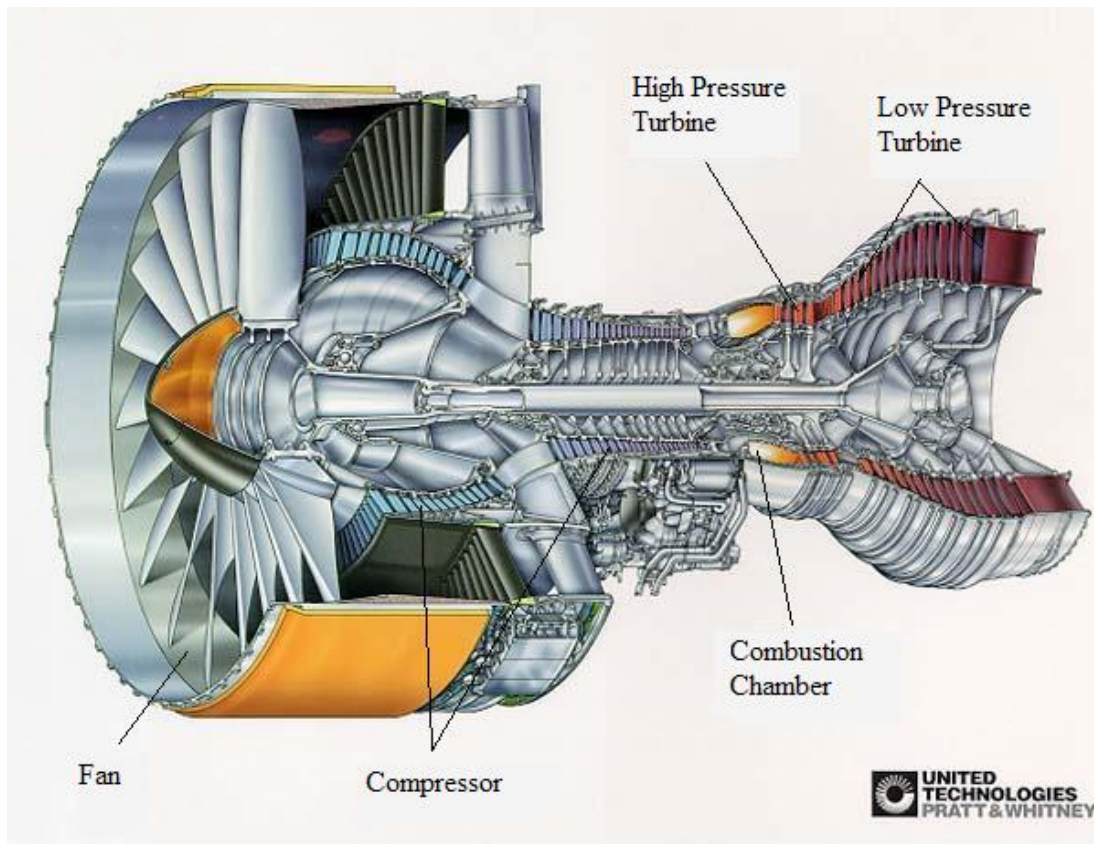


Figure 1: Schematic of a standard turbine engine for aircraft propulsion.

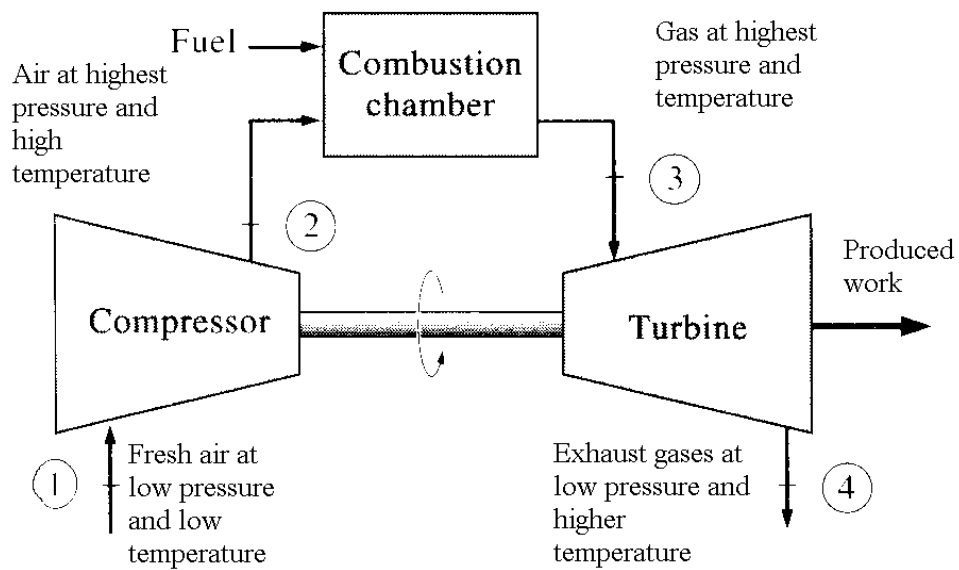


Figure 2: Thermodynamic cycle of a general turbine engine.

The temperature of the gas entering the turbine directly affects the power produced, and as the temperature increases, the efficiency of the turbine increases. The pressure ratio across the compressor is typically set to maximize the power output per unit mass. For an ideal engine, this pressure ratio is shown by Equation 1, where k is a ratio of specific heats of the gas and is approximately constant. The pressure ratio for an ideal compressor can also be expressed in terms of the temperature ratio across the compressor as in Equation 2. The thermal efficiency of the ideal engine is shown in Equation 3, and the power per unit mass can be expressed as in Equation 4.

$$r_p = \frac{P_2}{P_1} = \left(\frac{T_3}{T_1} \right)^{\frac{k}{2(k-1)}} \quad \text{Equation 1}$$

$$r_p = \frac{P_2}{P_1} = \left(\frac{T_2}{T_1} \right)^{\frac{k}{k-1}} \quad \text{Equation 2}$$

$$\eta_{th} = 1 - r_p^{\frac{k-1}{k}} \quad \text{Equation 3}$$

$$\frac{\text{power}}{\text{unit mass}} = C_p (T_3 - T_2) \eta_{th} \quad \text{Equation 4}$$

Substituting Equations 1 and 2 into 3 and 4, the efficiency and power can be expressed in terms of relevant temperatures. These relationships are shown through Equations 5 and 6, where η_{th} is engine efficiency, T_1 is the compressor inlet temperature, T_3 is the turbine inlet temperature, and C_p is the specific heat at constant pressure. In order to obtain a high efficiency and power output the turbine inlet temperature must be as high as possible.

$$\eta_{th} \approx 1 - \sqrt{\frac{T_1}{T_3}} \quad \text{Equation 5}$$

$$\frac{\text{power}}{\text{unit mass}} \approx C_p T_1 \left(\left(\frac{T_3}{T_1} \right)^{1/2} - 1 \right)^2 \quad \text{Equation 6}$$

The upper limit of the turbine inlet temperature depends on the material properties of the turbine blades. In order to increase this temperature, a protective layer can be added to the blades to increase their life. A common and effective process to protect the blades is to take relatively low temperature air from the compressor, route it through the machinery to inner cavities in the turbine blades, and expel it through angled holes machined in the blade surfaces. A representation of a turbine blade with cooling holes is depicted in Figure 3 (Sizov, 2003), and the image of the turbine rotor is shown in Figure 4 (Sizov, 2003). The cool air flows onto the blade surface as a film, hence the term film cooling. The hot post-combustion gas interacts with the cool film rather than the blade itself, which protects the blade. This allows for an increase in the operating temperature, T_3 , and thus the efficiency and power output of the engine. Currently, high performance gas turbines utilizing film cooling have turbine inlet temperatures of 2000K whereas the melting temperature of the blade material is approximately 1300K.

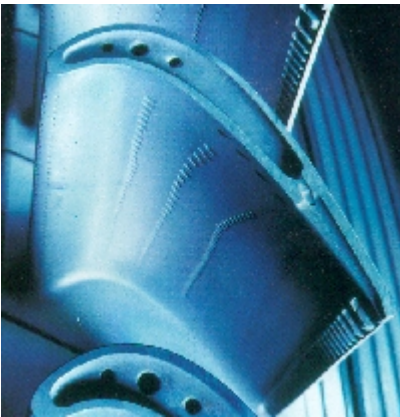


Figure 3: Turbine blade with cooling holes
Sizov (2003)

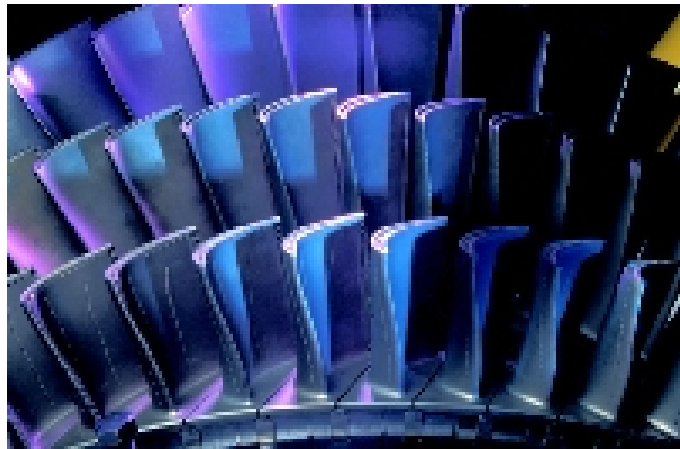




Figure 4: Series of rotating turbine blades. Sizov (2003)

The current applications of cooling use approximately twenty to twenty-five percent of the compressor air to cool the turbine blades (Ekkad *et al.* 2004), which reduces the ideal efficiency of the entire process by not routing as much air through the combustion chamber. Pulsing the bleed air could lessen the amount of required coolant air from the compressor significantly while still protecting the turbine blades. Interactions between a pulsed cool jet and a mainstream flow are not well understood, thus the amount of protection the pulsing would provide is unknown. An experimental study of the interactions between the coolant jets and mainstream flow will illuminate whether pulsing the bleed air provides enough protection for the blades to allow for the increase in efficiency.

Background

Film cooling has been studied extensively since the 1960's. Nearly all research has considered the behavior of a continuous stream of bleed air from the film cooling holes and its effectiveness in protecting the blade from the main flow. Many studies have been performed using simple flat plate geometries while varying film cooling parameters to gain more insight into the physics of the problem. LeBrocq *et al.* (1973) varied the coolant hole geometry and jet density in order to map the effects for multiple rows of staggered holes. Foster and Lampard (1980) showed that the angle of the jet hole significantly impacted the flow interactions. The mixing effects caused by flow turbulence were studied by Bons *et al.* (1994), who showed the importance of turbulence in the cooling process. As the freestream turbulence intensity was increased there was a proportionally higher mixing rate of the coolant and main flow. The mixing reduced the protection of the surface  to seventy percent in an area downstream of the coolant jet hole, yet improved the protection fifty to one hundred percent in the region between


coolant holes. More research pertaining to continuous film cooling can be found in VKI Lecture Series (1982) and Burd and Simon (2000).


Burd *et al.* (1998) analyzed the effects of varying the ratio between hole length to hole diameter and turbulence intensity. Wind tunnels with high and low freestream turbulence were used to blow air over a test section with a single row of eleven film cooling holes. Film cooling flow was injected at 35° to the surface, in line with the streamwise direction out of $D=1.9$ cm diameter holes separated 3 hole diameters (3D) apart. A square-edged rectangular polycarbonate strip was used as a trip  upstream of the hole centers to obtain a turbulent boundary layer. The ratios of length to diameter of the film cooling holes (L/D) were set to 7 and 2.3 and the freestream turbulence intensities (FSTI) were set to 0.5% and 12% of the freestream velocity. The flow was set so that the ratio of freestream velocity to jet velocity was one. The results showed that short-hole injection with low-FSTI spread the coolant more in the spanwise direction. High-FSTI diminished the effects of varying L/D distances. The apparatus used in the present study was based on that of Burd *et al.* (1998) to allow comparison of the baseline results of the present study using continuous film cooling.

Since film cooling will not perfectly protect a blade, there will be some heat transfer between the blade surface and the flow above it. The heat transfer is typically expressed in terms of a heat transfer coefficient, h , which is equal to the heat flux at the surface divided by the temperature difference between the surface and the mean flow temperature adjacent to the surface. To determine the heat transfer coefficient, surface heaters are typically used to provide a known uniform heat flux at the plate surface. Most of the previous flat plate experimental studies of heat transfer coefficients with film cooling have included an unheated starting length, with heaters only located downstream of the film cooling holes. An unheated starting length will

result in a thinner thermal boundary layer and higher heat transfer, but it is typically assumed that the ratio, h_f/h_o , will not be greatly affected by the presence of an unheated starting length. This is a ratio of the heat transfer coefficient with film cooling to the heat transfer coefficient in a similar flow without film cooling and the same surface heating. A study with an unheated starting length is Bons *et al.* (1996). While it is certainly plausible that an unheated starting length will affect a film cooled and uncooled boundary layer similarly, there is surprisingly little verification of the assumption in the literature. Mayhew et al. (2002) conducted experiments in a facility with a heated region upstream of the film cooling holes. They compared their results to data from similar studies with unheated starting lengths, and attributed differences observed in heat transfer coefficient ratios to unheated starting length effects. The heat transfer ratios were larger in the heated starting length cases. Mayhew et al. (2002) noted that since the thermal boundary layer is thicker in these cases, the film cooling flow may have more of an opportunity to disturb the thermal boundary layer and increase heat transfer. The only known study of unheated starting length effects is by Kelly and Bogard (2003). They considered full coverage film cooling on a flat plate with normal injection from multiple rows of holes. They present heat transfer coefficient ratios, h_f/h_o , at three streamwise locations downstream of the first row of holes for one of their cases. At $x=2D$, directly downstream of the holes, h_f/h_o was 30% higher with a heated starting length than with an unheated starting length. At $x=4D$ downstream of the holes, the effect was reduced, and by $x=10D$ downstream of the holes the heated and unheated starting length cases were indistinguishable. At the midspan between adjacent holes, the unheated starting length had no effect on h_f/h_o . No experimental results appear to be available in the literature for other geometries.


There are various possibilities as to the resulting interactions between a mainstream flow and a pulsed coolant jet. Although ideally the coolant will cover as much surface area when pulsed as well as provide a means to increase the efficiency of the turbine, there are several problems that may arise which need to be considered. Less air will be used in the cooling process which may result in insufficient coverage of the blade. However, if the pulsed coolant is able to cover the necessary blade area, then the efficiency may increase in the manner previously discussed. Another potential scenario is that the rapidly pulsed coolant air could result in more turbulence near the blade surface due to the cyclic process. The turbulence could cause rapid mixing of the mainstream and coolant flows. The mixing may allow higher temperatures to reach the blade surface, thus minimizing the effect of the coolant and potentially subjecting the airfoil to damage. The turbulence may also increase the heat transfer from the mainstream to the blade and possibly the cavity containing the coolant, causing the coolant jet to become ineffective. On the other hand, the mixing due to the turbulence may allow the coolant to distribute itself more effectively over the turbine blade, which in turn will allow for decreased heat transfer between the main flow and the blade surface. This series of events will allow the jet to effectively cool and protect the blade. Another advantage that may result from the pulsed coolant is a region of calm flow during the off portion of the jet cycle, following the turbulence caused by the jets (Bons *et al.*, 2002). This calm flow may have low turbulence and less mixing, which could result in a lower heat transfer between the mainstream flow and the blade surface. This phenomenon may protect the blade during the off portion of the coolant cycle.


There has been limited research on pulsed film cooling, with only three studies completed thus far. Two of these studies discussed the effects of pulsations due to engine unsteadiness, in which the jet flow was never turned off but was cyclically disturbed. s *et al.* (1996) used a

loudspeaker to induce pulsations in the jets and examined the effects of unsteadiness with a film cooling geometry similar to that of Burd *et al.* (1998). This study found that pulsations resulted in reduced film cooling effectiveness for low blowing ratios, which increased slightly as the blowing ratio increased to 1.5. Ligrani *et al.* (1996) used static pressure pulsations of the mainstream flow generated by an array of rotating shutter blades. This study showed that pulsations cause the film cooling jet to spread more uniformly across the test surface. The spreading was caused by the jet flow oscillating in both the normal and spanwise directions as it left the hole. Ekkad *et al.* (2004) examined the effects of controlled pulsed film cooling through the use of solenoid valves. A single film cooling hole angled 20° to the spanwise direction and 90° to the streamwise direction was located on the leading section of a cylinder. This study determined that pulsed jets increase the ability to effectively protect the surface and slightly lower  transfer coefficients compared to a continuous jet.

Modeling

Conservation of mass, conservation of momentum, and conservation of energy govern the flow and heat transfer of any system. These laws are expressed by differential equations which are too complex to solve analytically for turbulent flow; no known solutions exist. In theory they can be solved numerically, however only relatively simple flows can be solved using the most advanced computers.

Hence, the solution to the equations for a flow including the effects of pulsing on film cooling can only be determined through experimentation. A scaled apparatus was constructed to produce a flow that is representative of the flow over a row of film cooling holes on a gas turbine blade.  The important dimensionless numbers appearing in the governing equations are matched between the prototype turbine blade and the experimental flow, then the governing equations

describing the flow over a gas turbine airfoil will match the equations describing the flow over a geometrically similar experimental apparatus. Once the dimensionless equations match, the resulting dimensionless solutions will also match. The solution is the velocity and temperature fields describing the flow.  of the dimensionless numbers that must be matched is the Reynolds number, Re , which helps distinguish between laminar and turbulent flow. The Reynolds number is defined as the ratio of the inertia force on an element of fluid to the viscous force on an element (Munson et al, 2002), as shown through Equation 7,

$$Re_{\text{model}} = Re_{\text{engine}}$$

$$\left[\frac{VD_{\text{hole}}}{\nu} \right]_{\text{model}} = \left[\frac{VD_{\text{hole}}}{\nu} \right]_{\text{engine}} \quad \text{Equation 7}$$

where V is the velocity of the main flow over the coolant hole, D is the diameter of the coolant hole, and ν is the kinematic viscosity of the fluid. If the Reynolds number is very small, the viscous forces are dominant in the flow; conversely, if the Reynolds number is large, the viscous effects are small relative to inertial effects.

The second nondimensional number appearing in the dimensionless governing equations is the Prandtl number, Pr , which is a property of the fluid. The Prandtl number for air is approximately 0.73 (Lakshminarayana, 1996), and it is the ratio of kinematic viscosity to thermal diffusivity of the fluid. This number will remain constant throughout the analysis because the numerical ratio is the same for air and combustion gases. The Prandtl number is shown in Equation 8, where α is the thermal diffusivity.

$$Pr_{\text{model}} = Pr_{\text{engine}}$$

$$\left[\frac{\nu}{\alpha} \right]_{\text{model}} = \left[\frac{\nu}{\alpha} \right]_{\text{engine}} \quad \text{Equation 8}$$

The velocities of the main flow and coolant jet were based upon matching the blowing ratios of the model and prototype. The blowing ratio, B , is the ratio of the coolant jet velocity and density to the mainstream velocity, V_∞ , and density, as shown in Equation 9. In the experimental apparatus, the jets are only heated to approximately 7°C above the mainflow temperature. This causes the density ratio of jets to mainflow to be approximately 0.98, hence the blowing ratio can be reduced to the velocity ratio.

$$B_{\text{model}} = B_{\text{engine}}$$

$$\left[\frac{V_{\text{jet}} \rho_{\text{jet}}}{V_\infty \rho_\infty} \right]_{\text{model}} = \left[\frac{V_{\text{jet}} \rho_{\text{jet}}}{V_\infty \rho_\infty} \right]_{\text{engine}} \quad \text{Equation 9}$$

$$\left[\frac{V_{\text{jet}}}{V_\infty} \right]_{\text{model}} = \left[\frac{V_{\text{jet}}}{V_\infty} \right]_{\text{engine}}$$

The Mach number, M , represents the compressibility effect, which is the ratio of inertial forces to compressibility forces. This is shown in Equation 10, where c is the speed of sound.

$$M = \frac{V_\infty}{c} \quad \text{Equation 10}$$

Ideally, the Mach numbers of the model and prototype flows would also be equivalent; however, these numbers were impossible to match in this laboratory experiment. The practice of ignoring the Mach number effect is acceptable for film cooling experiments, as the Mach number is not as important to match as compared to the Reynolds number, and most of the existing data and analysis of film cooling is based on this assumption.

A similar dimensionless solution for the model and prototype turbine blade flows was insured by matching the Reynolds number, Prandtl number, and blowing ratios. The dimensionless solution can be expressed in terms of the film cooling effectiveness and the Stanton number. The film cooling effectiveness, η , is a form of the dimensionless temperature

solution, and is computed from the measured temperatures in the model flow. The film cooling effectiveness is a measure of how well the jet cools the plate, ranging from zero to one, with one being the best. Equation 11 shows the film cooling effectiveness, where T_∞ is the temperature of the freestream flow, and T_{jet} is the temperature of the coolant jet. The subscript ‘aw’ stands for ‘adiabatic wall;’ T_{aw} would be the wall temperature if there was no convective heat transfer from the wall. The adiabatic wall temperature would equal the jet temperature if the jet were operating ideally; that is, the temperature of the plate would be equal to the temperature of the jet.

$$\eta_{model} = \eta_{engine}$$

$$\left[\frac{T_{aw} - T_\infty}{T_{jet} - T_\infty} \right]_{model} = \left[\frac{T_{aw} - T_\infty}{T_{jet} - T_\infty} \right]_{engine} \quad \text{Equation 11}$$

Similarly, the Stanton number, St , is also equal for the model and prototype if the Reynolds number, Prandtl number, and blowing ratio are matched. It represents the nondimensional heat flux from the flow onto a surface as shown in Equation 12. The Stanton number for the model is determined by setting the heat flux, q'' , as supplied by electric heaters, and measuring the wall temperature and flow velocity. The relationship is shown in Equation 12, where ρ is the density of the fluid, C_p is the specific heat of the fluid, T_{wall} is the plate temperature, and V_∞ is the main flow velocity.

$$St_{model} = St_{engine}$$

$$\left[\frac{q''_{conv}}{\rho C_p V_\infty (T_{wall} - T_{aw})} \right]_{model} = \left[\frac{q''_{conv}}{\rho C_p V_\infty (T_{wall} - T_{aw})} \right]_{engine} \quad \text{Equation 12}$$

To determine the film cooling effectiveness and Stanton number for the model flow, two tests were conducted for each experimental condition. The surface temperature, heat flux, and

temperatures were measured with the plate unheated, and with the wall heaters on. The convective heat flux is determined based on an energy balance at the plate surface, as shown in Equation 13, where ε is the surface emissivity, σ is the Stefan-Boltzmann constant, T_{surr} is the temperature of the surroundings, k is the thermal conductivity of the test surface, T_{heaters} is the average temperature of the heaters, T_{back} is the temperature of the back of the plate, and t is the thickness of the plate.

$$q''_{\text{conv}} = q''_{\text{heaters}} - q''_{\text{rad}} - q''_{\text{cond}}$$

$$q''_{\text{conv}} = q''_{\text{heaters}} - \varepsilon \sigma (T_{\text{wall}}^4 - T_{\text{surr}}^4) - k \frac{T_{\text{heaters}} - T_{\text{back}}}{t} \quad \text{Equation 13}$$

If the radiation and conduction corrections are subtracted from the heat flux the heaters are producing, the convective heat flux remains. This was determined for both the unheated and heated cases. In order to calculate the film cooling effectiveness, Equation 11 is solved for T_{aw} , and then substituted into Equation 12. The Stanton numbers for the unheated and heated cases are set equal to each other, since the convective heat transfer coefficient remains constant regardless of the heater condition. The equations are then solved for the Stanton number and film cooling effectiveness.

In a gas turbine hot gases comprise the mainstream flow, the blades are cooled, and relatively cold coolant jets provide the film cooling. The goal is to maintain minimal heat transfer between the blade surface and the flow over the blade. If the temperature difference between the blade surface and the adjacent fluid is small, as is the case when the majority of the adjacent fluid is the cool air from the film cooling holes, the heat transfer rate will be low and the film cooling process works. The opposite is true for high heat transfer, where the temperature difference between the surface and the adjacent fluid is great because the fluid directly above the blade is mostly the hot combustion gases. In the present study the temperature differences were

analogous but opposite. The mainstream flow was cool, the test surface was hot, and the film cooling jets were warm. Heat always flows from hot to cold, so when the temperature difference ($T_{\text{wall}} - T_{\text{aw}}$) changes signs, the heat flux, q'' , also changes signs. Hence the sign of the Stanton number is unchanged, and the Stanton numbers for the model and engine remain equal, regardless of the direction of heat flow in each.

In order to better compare the results of separate tests the Stanton number ratio is used. The Stanton number ratio is a non-dimensional number that reduces differences associated with various facilities or parameters. It compares the Stanton number for a particular blowing and heating case, St_f , to the Stanton number of the case with no blowing and the same heating configuration, St_o .

There are now two important non-dimensional numbers presented to determine the best case of film cooling: the film cooling effectiveness and the Stanton number ratio. However, some results may show a certain case to have improved the film cooling effectiveness, but not the Stanton number, or vice versa. The film cooling effectiveness can improve if the jet remains closer to the plate and the temperature difference between T_{aw} and T_{jet} is small. However, increased turbulence, increased mixing of the jet and mainstream flows, and the jet impinging on the surface can increase the heat transfer between the surface and the adjacent flow, thus worsening the Stanton number ratio. In order to determine the overall film cooling performance the heat flux ratio is used. The heat flux ratio takes into account the effects of the film cooling effectiveness and the Stanton number ratio, as shown in Equation 14.

$$\frac{q''_f}{q''_o} = \frac{St_f}{St_o} \left(1 - \frac{\eta}{0.6} \right) \quad \text{Equation 14}$$

The constant 0.6 in Equation 14 represents a dimensionless temperature ratio $(T_{\text{wall}} - T_{\infty}) / (T_{\text{jet}} - T_{\infty})$ that results from the combination of Equations 11 and 12. The numerical value of 0.6 is taken from Jung *et al.* (2002), and is a typical value for this temperature ratio under engine conditions. The best possible film cooling case would have a heat flux ratio of zero. This could theoretically be achieved if η was 0.6 or greater. In this study, film cooling effectiveness above 0.6 are found in some cases, resulting in a negative heat flux ratio. Theoretically, the best case would then be the one with the smallest heat flux ratio. Typically, the film cooling effectiveness has a larger effect on the heat flux ratio than the Stanton number ratio, primarily because the Stanton number ratio is typically close to one.

Experimental Facilities

Experiments were conducted with an open loop subsonic wind tunnel with a test plate attached at the exit, and a plenum to supply the film cooling jets. The wind tunnel, shown in Figure 5, was comprised of six sections: a blower, a diffuser with three screens, a heat exchanger to maintain air nominally at 20°C, a honeycomb, a settling chamber with three screens, and a nozzle with an 8.8 area reduction. The nozzle exit area is 0.38 m x 0.10 m. The exiting mainstream air was uniform in temperature and velocity to within 0.1°C and 1% respectively. The freestream turbulence intensity at the nozzle exit was 1%. Air exiting the nozzle formed a wall jet at $V_{\infty} = 8$ m/s along a flat plate which served as the test wall. The velocity was controlled via an AC variable frequency drive used to set the blower motor speed. The mainstream velocity remained at 8 m/s 19.5D downstream from the leading edge of the film cooling holes with the freestream unsteadiness level increasing gradually to 6%. The wall jet configuration is based on the facility of Burd and Simon (2000). Figures 6-11 depict the individual sections of the wind tunnel. Figure 6 is a picture of the blower and Figure 7 is a picture of the AC variable frequency

driver which controls the speed of the motor that drives the blower shaft. Figure 8 is an image of the diffuser. Figure 9 shows the heat exchanger and settling chamber. Figure 10 is a photograph of the nozzle, and Figure 11 shows the nozzle connecting to the test plate.

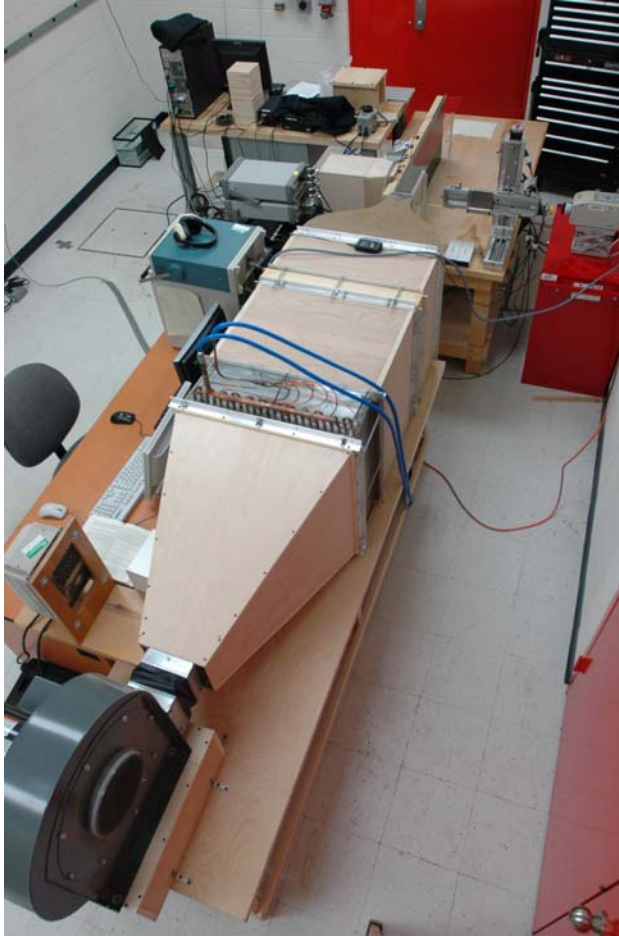


Figure 5: Wind tunnel.

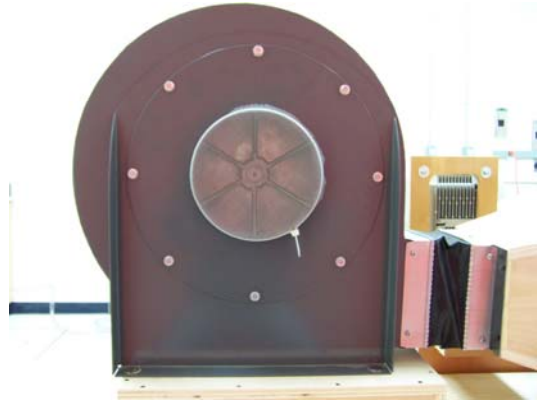


Figure 6: Blower.



Figure 7: AC variable frequency driver.



Figure 8: Diffuser.

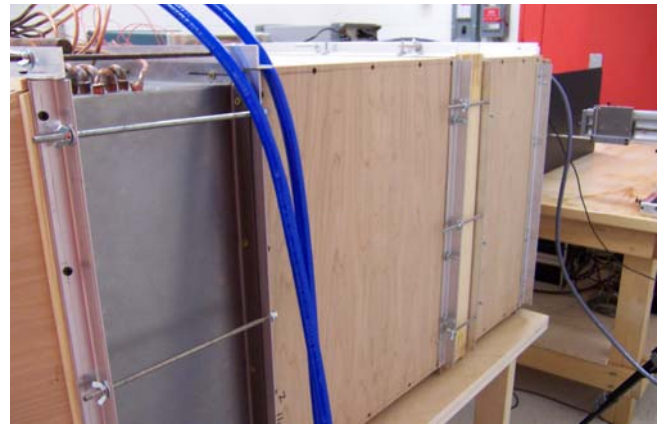


Figure 9: Heat exchanger and settling chamber.

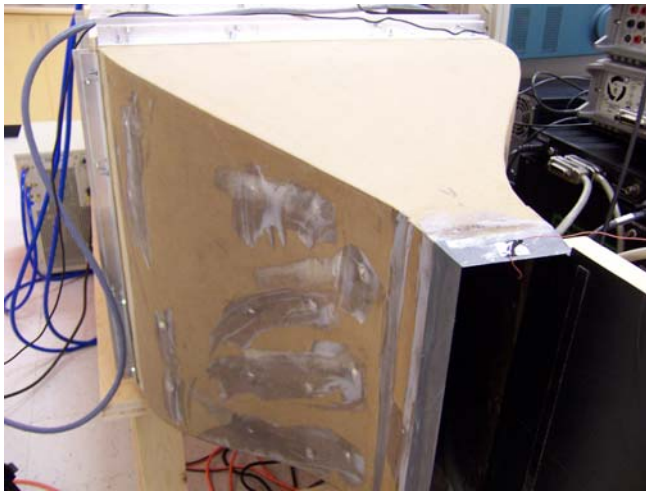


Figure 10: Nozzle.



Figure 11: Nozzle connecting to test plate.

The test wall was constructed of polyurethane foam with a thermal conductivity of 0.027 W/mK . The dimensions were 0.38 m wide, 44 mm thick, and 1.17 m long, with a starting length of $13.3D$ upstream of the row of film cooling holes. A wall opposite the starting length and side walls along the length of the test wall helped limit interaction between the wind tunnel flow and the still air in the room, as shown in Figure 12. Metal foil heating elements encapsulated in silicon rubber coatings (Minco, Inc.) were placed on the foam surface as shown in Figure 13. There was one $25.4\text{cm} \times 38.1\text{cm}$ heater upstream of the film cooling holes, two $2.54\text{cm} \times 5.08\text{cm}$ heaters on the outside of the holes, four $2.54\text{cm} \times 2.54\text{cm}$ heaters between the holes, and three

25.4cmx38.1cm heaters downstream of the holes. Each test was first run with the plate unheated, then with the upstream and downstream heaters on for use in calculating the film cooling effectiveness and Stanton number. In order to determine the effects of an unheated starting length tests were run with only the downstream heaters on, with the upstream and downstream heaters on, and with all the heaters on. The heaters were covered with a 0.79 mm thick black sheet of Formica® laminate to provide a smooth test surface. The heaters provided a heat flux which was uniform to within 1.4%. Any small spatial non-uniformity in the heat flux at the test surface was quantified by examining the local surface temperature in a case with no film cooling and the cooling holes taped over (i.e. simple flow over a flat plate with an unheated starting length). This allowed for correction of the local heat flux in all subsequent tests for computation of Stanton numbers. Stanton number ratios were unaffected by the corrections, since the corrections canceled when the ratios were computed. The film cooling geometry consisted of a single row of five round holes inclined at 35° to the surface and parallel to the streamwise direction. The sharp edged holes had a diameter of $D=19.05$ mm spaced $3D$ apart, center to center, and with a length to diameter ratio $L/D=4$. A 1.6 mm thick trip was installed $11D$ upstream of the leading edge of the film cooling holes to ensure a turbulent boundary layer. This geometry was based on a similar film cooling study by Burd et al (1998). Figure 14 shows the row of five film cooling holes.



Figure 12: Wall opposite the starting length and side walls.

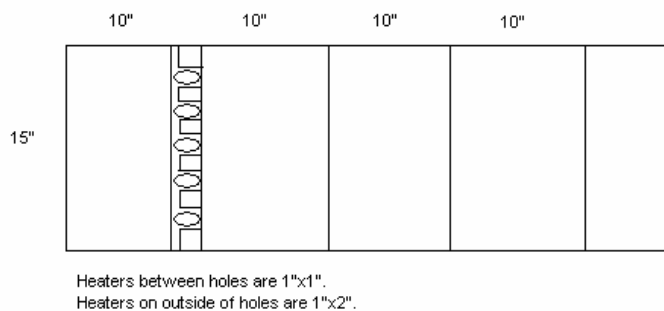


Figure 13: Heater configuration.

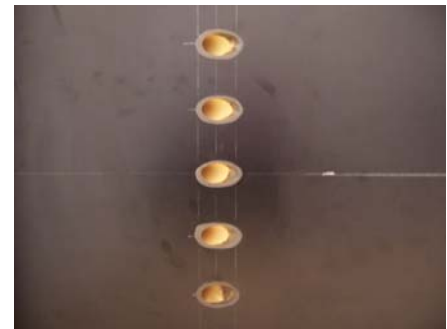


Figure 14: Film cooling holes.

The film cooling supply plenum was supplied by a manifold connected to a high pressure air source. The supply pressure was adjusted to vary the blowing ratio from $B=0.25$ to 1.5. The air passed through small diameter solenoid valves between the manifold and the plenum. The valves were used for both continuous and unsteady film cooling. The solenoid valves open and close via electric pulse and can transfer air up to 690 kPa (100 psi). The flow through the valves was choked. For a given supply pressure, the film cooling mass flow remained constant, independent of downstream conditions. The relationship between the supply pressure and the jet velocity is shown in Equation 15, which was determined via hot wire testing.

$$\text{Jet Velocity (m/s)} = 0.564 + 0.0117 \cdot \text{Supply Pressure (kPa)} \quad \text{Equation 15}$$

The plenum had a finned tube heat exchanger to maintain the temperature of the coolant jets at approximately 26°C. Warm water at 30°C circulated through multiple tube passes of the heat exchanger. The jet air from the valves passed over the tubes in a cross-flow manner, which caused heat transfer from the hot water in the tubes to the jet flow. Figure 15 shows a side view of the cooling tank supply plenum, Figure 16 is a depiction of the solenoid valves, with Figure 17 showing a single valve, and Figure 18 shows all the equipment that runs the solenoid valves and the heat exchangers.

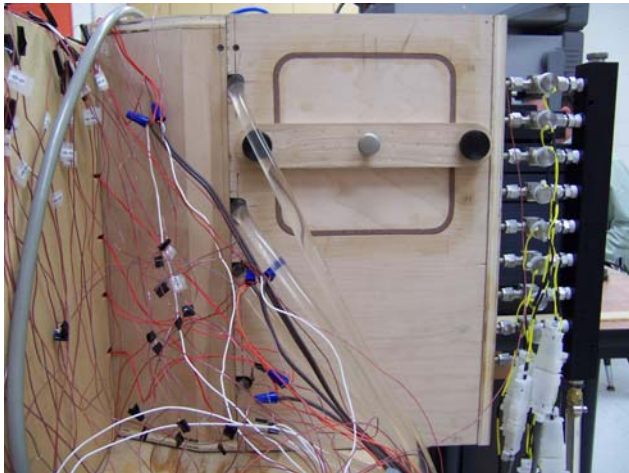


Figure 15: Film cooling tank supply plenum.

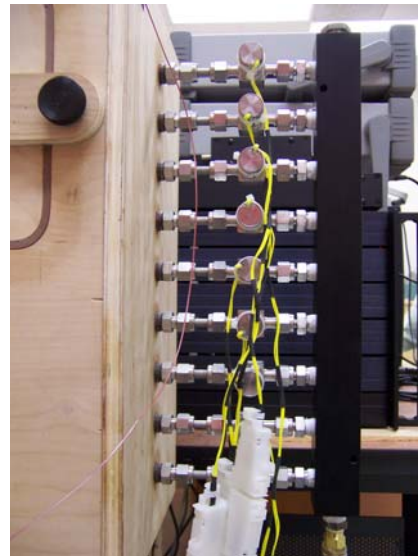


Figure 16: Solenoid valves.



Figure 17: Single solenoid valve.

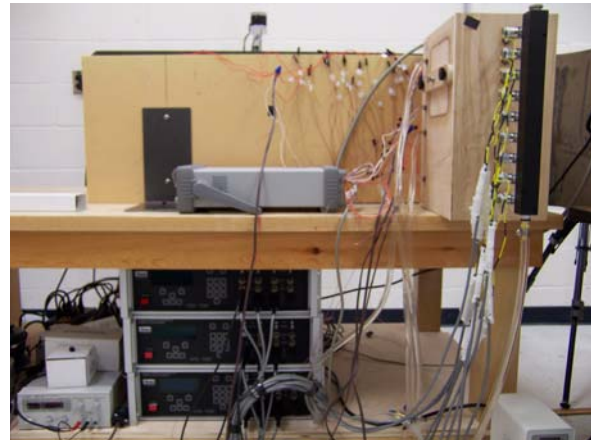


Figure 18: All cooling tank equipment.

Instrumentation

The equipment used to measure temperature and velocity is illustrated in Figure 19, which includes thermocouples, a hot wire anemometer, a cold wire anemometer, and an Infrared camera.

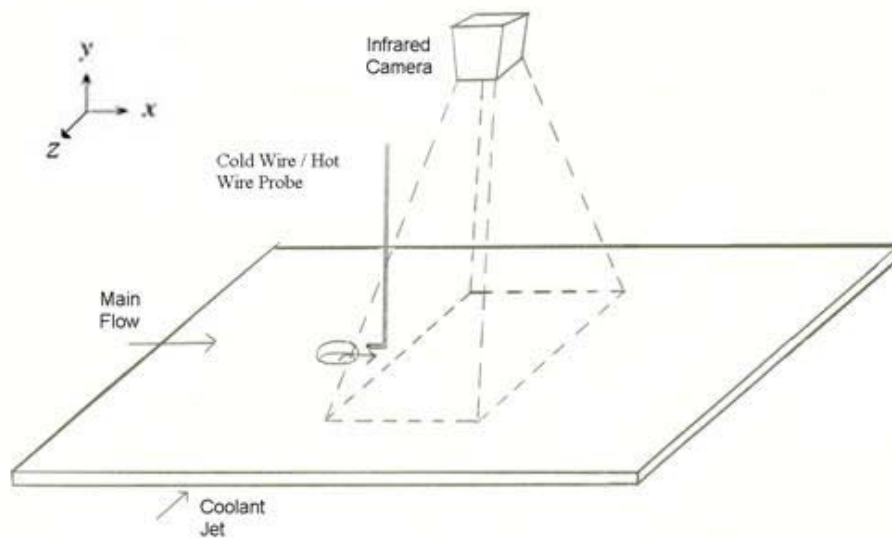


Figure 19: Measuring devices.

Thermocouples are used to measure temperature at a point. A thermocouple is made of two dissimilar metals, usually in the form of wires that are joined at one end by soldering or

welding to form a junction. A voltage is produced when there is a temperature difference between this measuring junction and the opposite ends of the wires, which are connected to a voltmeter. The magnitude of the voltage is related to the magnitude of the temperature difference. The test plate was instrumented with Type E thermocouples of 76.2 μm diameter wire. The thermocouples were located between the heaters and Formica, which was attached with an epoxy. Thermocouples were also placed in the film cooling plenum, in one of the outside film cooling holes, at the wind tunnel exit, on the back of the test plate, in the ambient air, on the wall of the room to measure the surrounding temperature for radiation corrections, and in ice water as a reference. Figure 20 is a depiction of a single thermocouple, and Figure 21 shows the thermocouple distribution on the test plate.



Figure 20: Single thermocouple.

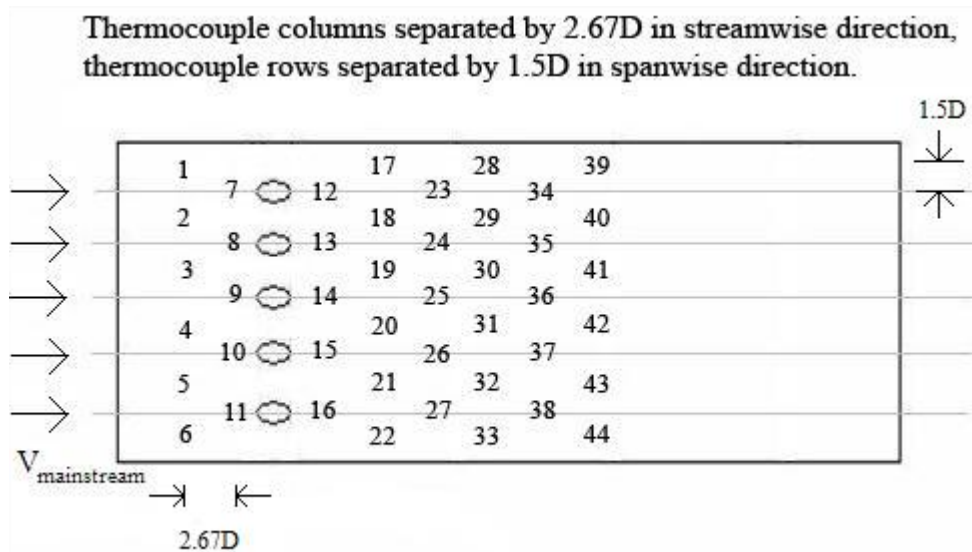


Figure 21: Thermocouple distribution on test plate.

A hot wire measures the instantaneous velocity of the flow. A circuit is used to hold the wire at a specific temperature, and the wire is placed in a flow, which attempts to cool the wire. Temperature is proportional to resistance, thus a constant resistance is held across the wire and the flow attempts to vary that resistance. The voltage varies in order to maintain a constant resistance, and the change in voltage is used to determine the velocity of the flow. Equation 16 shows the calibration equation relating voltage to velocity of the flow. Fluctuations in the velocity about the mean indicate the turbulence level. Boundary layer probes with 3.81 μm diameter tungsten sensors (TSI model 1218-T1.5) were used for the velocity measurement.

$$velocity = \left(A + B \times voltage^2 \right)^{\frac{1}{C}} \quad \text{Equation 16}$$

A cold wire probe measures the instantaneous temperature in the flow via a current-carrying wire which acts as a resistance temperature detector. A very low constant current travels through the wire. The wire temperature changes with the temperature of the flow passing around it, and the electrical resistance of the wire is directly proportional to its temperature. The voltage across the wire changes in response to the varying resistance. The voltage change is measured and converted to temperature via the calibration equation shown below. Boundary layer probes with 1.27 μm diameter platinum sensors (TSI model 1261A-P.5) were used for temperature measurements.

$$temperature = A \times voltage + B \quad \text{Equation 17}$$

The hot and cold wire probes are held in a probe holder which does not interfere significantly with the flow, and the holder is connected to a three axis traverse. The probes can thus traverse along the majority of the plate while creating minimal flow disturbance. Figure 22 shows a hot wire, Figure 23 shows a cold wire, figure 24 is a depiction of the probe holder, and Figure 25 is an image of the three axes traverse.

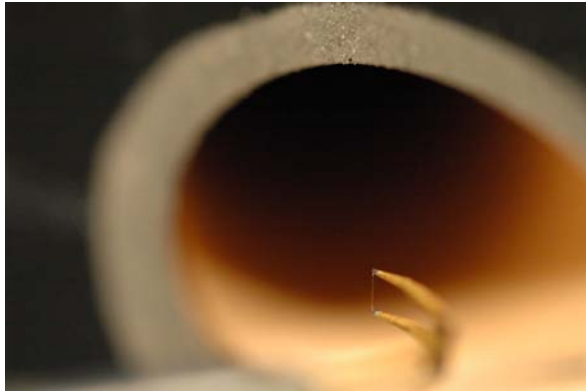


Figure 22: Hot wire.

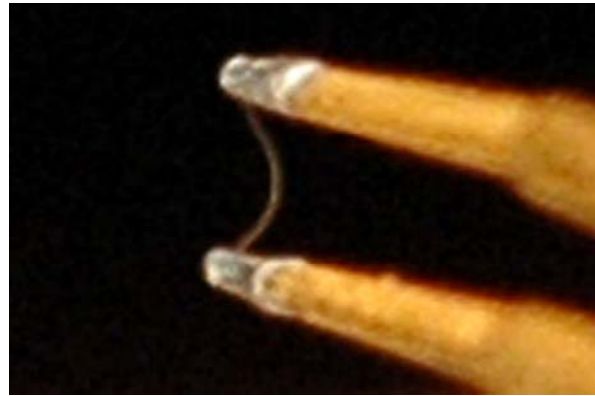


Figure 23: Cold wire.

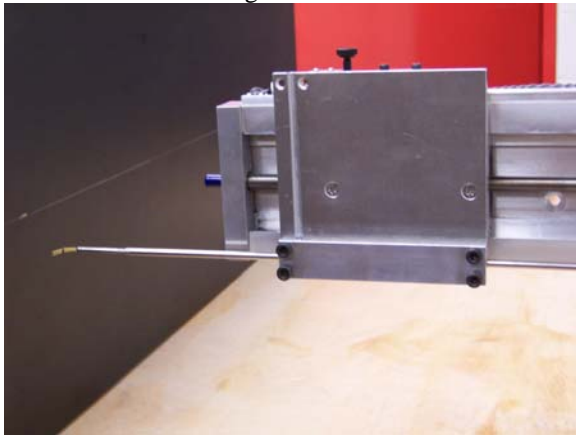


Figure 24: Probe holder.

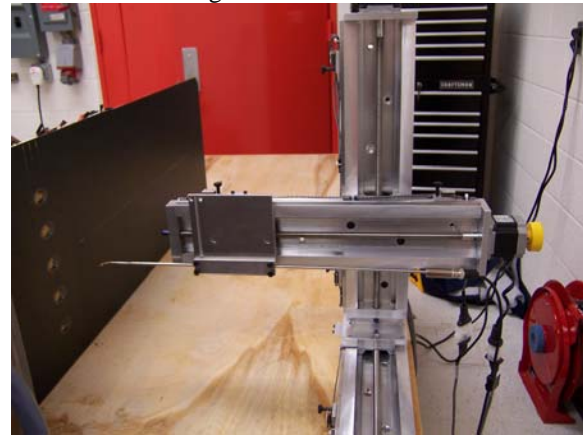


Figure 25: Three axes traverse.

An Infrared (IR) camera (FLIR Systems Merlin model) (Figure 26) with a Stirling cooled detector was used to measure the surface temperature field of the test wall. The temperature resolution of the camera is 0.05°C . The temperature range of the camera is set such that very small temperature differences are detectable on the plate surface. The camera has a 255×318 pixel detector and was positioned such that each pixel corresponded to a $1\text{ mm} \times 1\text{ mm}$ area on the test wall. The field of view on the test wall corresponded to $11D \times 14D$. The emissivity of the test wall was determined to be 0.95 through comparison of IR images of the test wall and a surface of known emissivity (black electrical tape) at the same temperature. The thermocouple array in the plate was also checked, however could not be used for accurate emissivity calculations because there could have been a small change in temperature between the

thermocouples under the Formica and the surface. Figure 27 is an image of a hand to show the sensitivity of the camera.

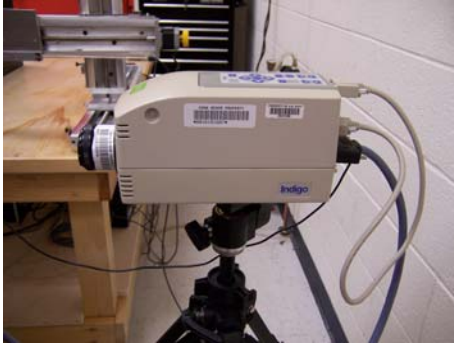


Figure 26: IR camera.

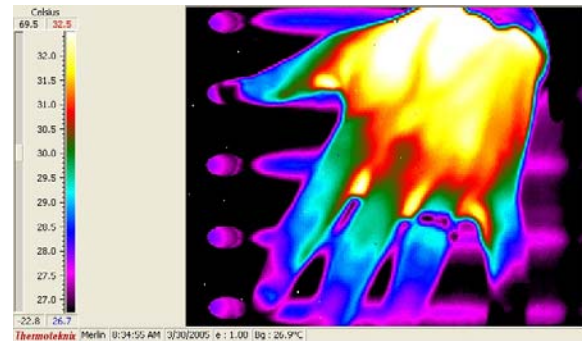


Figure 27: Image to show camera sensitivity.

Boundary layer parameters were measured to quantify the mainstream flow. The boundary layer 0.8D upstream of film cooling hole leading edge had a momentum thickness Reynolds number of 810 and a shape factor of 1.5. The local skin friction coefficient at this location was $C_f = 4.8 \times 10^{-3}$. With the upstream heaters active, the enthalpy thickness Reynolds number 0.8D upstream of the holes was 600. These are parameters used to characterize the boundary layer and can be used to compare the flow to other studies.

The film cooling jet flow uniformity was measured by traversing the cold wire (temperature) and hot-wire (velocity) probes over the hole exit with the main flow in the wind tunnel off. Figure 28 shows the temperature distribution for a jet flow corresponding to blowing ratio $B=0.5$. The jet temperature was clearly very uniform and matched the plenum temperature to within 0.2°C . The temperature distribution was checked for all blowing ratios and found to be uniform in all cases. Figure 29 shows the mean velocity for the jet flow in the $B=0.5$ case. The higher velocity region in the upstream section of the hole was due to the flow pattern of the jet from the plenum, through and out of the hole. Burd and Simon (2000) discuss jet velocity distribution in similar configurations in more detail. The jet velocities were averaged over the hole exit to determine an average velocity. The jet velocity distribution will no doubt change

when the main flow is turned on, but the mean velocity will remain the same since the flow rate is set by the choked mass flow through the upstream solenoid valves.

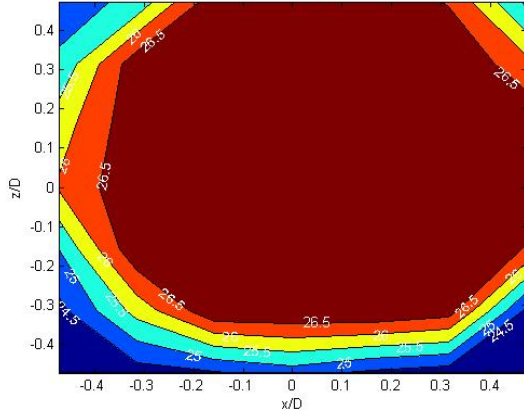


Figure 28: Temperature profile of center hole at B=0.5.

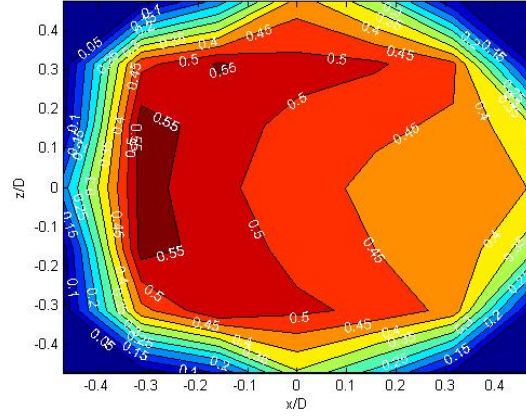


Figure 29: Velocity profile of center hole at B=0.5.

The uncertainty in the measured temperature was 0.2°C , the uncertainty in the measured velocity was 3%, and the uncertainty in the atmospheric pressure was 1%. The uncertainties in the film cooling effectiveness and the Stanton number were determined using standard propagation of error. The uncertainty in the film cooling effectiveness was 6% and the uncertainty in the Stanton number was 8%. The uncertainty in the ratio of two Stanton numbers was 11%.

Results

The experimental results of this study included baseline tests with no film cooling, continuous film cooling with varying blowing ratio, the effect of an unheated starting length, and pulsed film cooling with respect to varying frequency and duty cycle. A test matrix is shown in Table 1.

	B=0.125	B=0.25	B=0.5	B=1.0	B=1.5
No Blowing					
Continuous Blowing					
No heating	x	x	x	x	x
Downstream heating	x	x	x	x	x
Downstream/Upstream heating	x	x	x	x	x
Full heating	x	x	x	x	x
Pulsing - Varying Frequency					
F=10Hz DC=0.5		x	x	x	x
F=20Hz DC=0.5		x	x	x	x
F=80Hz DC=0.5			x		
Pulsing - Varying Duty Cycle					
F=20Hz DC=0.25			x	x	
F=20Hz DC=0.75			x	x	

Table 1: Test matrix.

Baseline Results – No Film Cooling

Baseline results were acquired with no film cooling. For these experiments the film cooling holes were covered with tape. Four no blowing cases were run with a mainstream velocity of $V_\infty=8$ m/s and a combination of heater configurations: an unheated surface, heating downstream of the film cooling holes, heating upstream and downstream of the holes, and heating on all the locations of the test wall. Stanton number distributions (St_o) were determined for the three heated cases. Stanton numbers were also computed using a boundary layer code (TEXSTAN, Crawford and Kays, 1976) using a mixing length turbulence model and heat transfer boundary conditions to match the three experimental cases. The calculated and experimental Stanton numbers agreed to within 5%. At 2D downstream of the film cooling holes, the Stanton numbers with upstream heating were approximately 35% higher than those with an unheated starting length. The difference decreased to 19% 13D downstream of the holes. The effect of the small heaters between the film cooling holes was small and was only discernable within 3D downstream of the film cooling holes. This was true both with and without film cooling. Hence, this case is not presented below, and the focus is on difference

between the cases with only downstream heating and heating upstream and downstream of the holes.

Continuous Film Cooling Results – Film Cooling Effectiveness

Continuous film cooling was studied with blowing ratios of $B=0.125$, 0.25 , 0.5 , 1.0 , and 1.5 . These tests helped determine the effect of varying blowing ratio, as well as establish comparison cases for the pulsing cases. The film cooling effectiveness was computed for each of these cases. Figure 30 is the film cooling effectiveness contour plot for a blowing ratio of $B=0.125$. It shows the five film cooling holes on the left side with the origin at the downstream edge of the center film cooling hole. The ordinate is the spanwise distance across the surface measured in hole diameters, and the abscissa is the streamwise distance measured in diameters as well. Red represents high film cooling effectiveness, and blue shows low film cooling effectiveness. For the blowing ratio of $B=0.125$ the jet velocity was low enough so that it remained on the wall at the hole exit and protected the plate directly downstream of the film cooling holes. However, the film cooling effectiveness decreased dramatically after $2D$ downstream. In order to further show the trend in film cooling effectiveness, the data taken at $z/D=0$, or the center line of the middle hole, was plotted versus x/D in Figure 31. The film cooling effectiveness was high directly downstream of the holes, but dropped considerably thereafter. In order to sufficiently protect a turbine blade with this continuous blowing ratio, additional rows of holes need to be added to maintain a high enough film cooling effectiveness over the surface. This would ultimately increase the amount of mass needed for film cooling, showing that a continuous blowing ratio of $B=0.125$ is not the best choice. Therefore, this blowing ratio was not investigated any further in this study.

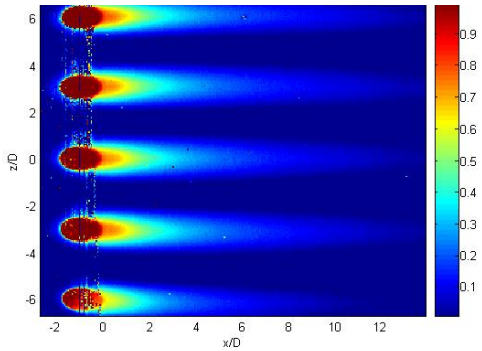


Figure 30: Film cooling effectiveness contour plot for B=0.125 continuous

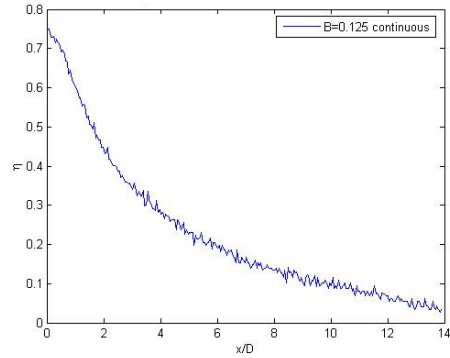


Figure 31: Centerline film cooling effectiveness for B=0.125 continuous

Continuous blowing at a ratio of $B=0.25$ showed a high film cooling effectiveness further downstream of the holes. This is seen in Figures 32 and 33, where the effectiveness starts high and slowly decreases. The blowing ratio of $B=0.5$ also showed the same positive results, with a high film cooling effectiveness along the length of the test surface (Figures 34 and 35). However, the blowing ratio of $B=0.25$ used less mass than the $B=0.5$ case, and is thus more ideal for film cooling.

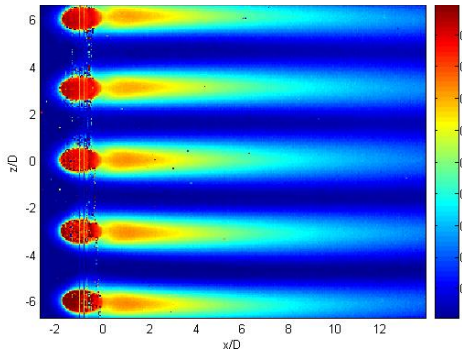


Figure 32: Film cooling effectiveness contour plot for B=0.25 continuous

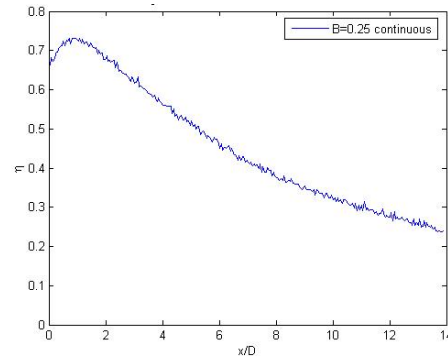


Figure 33: Centerline film cooling effectiveness plot for B=0.25 continuous

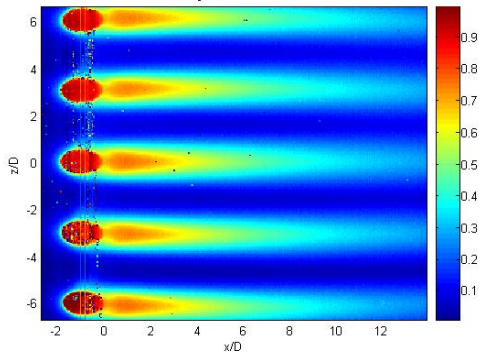


Figure 34: Film cooling effectiveness contour plot for $B=0.5$ continuous.

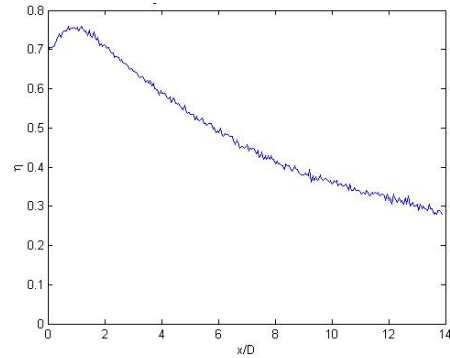


Figure 35: Centerline film cooling effectiveness plot for $B=0.5$ continuous

The cases of continuous blowing at $B=1.0$ and $B=1.5$ showed much lower film cooling effectiveness due to jet lift off as shown in Figures 36-39. This was a result of the jet velocities being so high that the jet separated from the test surface, increasing the possibility of mixing the fluid streams, resulting in increased heat transfer. The mainstream flow pushed the jet back onto the surface further downstream, providing less effective protection since the jet has already been mixed with the mainstream flow. The film cooling effectiveness was thus low directly downstream of the holes and then rose somewhat as the jet reattached to the surface at approximately $3D$ downstream for $B=1.0$ and $5D$ downstream for $B=1.5$.

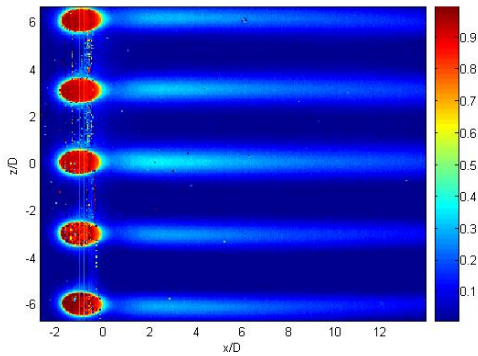


Figure 36: Film cooling effectiveness contour plot for $B=1.0$ continuous

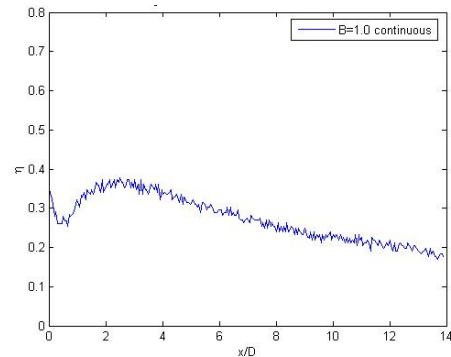


Figure 37: Centerline film cooling effectiveness plot for $B=1.0$ continuous

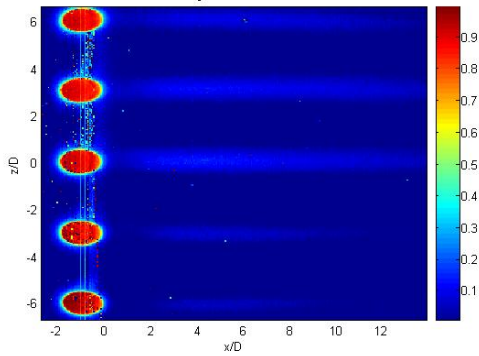


Figure 38: Film cooling effectiveness contour plot for $B=1.5$ continuous

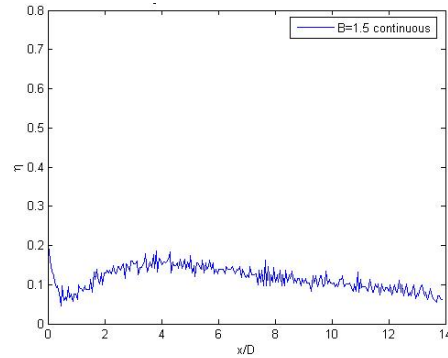


Figure 39: Centerline film cooling effectiveness plot for $B=1.5$ continuous

Jet lift off was also shown through a cold wire survey of the flow in planes downstream of the center film cooling hole at three streamwise locations. The cold wire was traversed in planes at $x=3.5D$, $7D$, and $14D$ extending from the surface ($y/D=0$) to $y=2.5D$ and across the span from $z=-1.5D$ to $1.5D$, as shown in Figure 40, yielding the planar temperature distribution. The time averaged temperatures of the flow within those planes were plotted to demonstrate the jet flow behavior. Figures 41-43 show the jet flow of $B=0.25$ at the locations $x=3.5D$, $7D$, and $14D$ respectively. Figures 44-46 are of the same planes for the blowing ratio of $B=0.5$. As seen in Figures 41 and 44, the jet flow for low blowing ratios remained close to the test surface at $x=3.5D$, thus resulting in a high film cooling effectiveness directly downstream of the holes. As the flows traveled further downstream, the jet inevitably spread and began to mix with the mainstream flow. Yet at these distances further downstream of the holes the jet remained relatively close to the surface. Figures 47-49 show the temperature planes for $B=1.0$, and Figures 50-52 are for $B=1.5$. Figure 47 shows that the jet for $B=1.0$ had already separated from the surface at $x=3.5D$, and Figure 50 shows that $B=1.5$ worsened the lift off effect. As these jets traveled further streamwise, they spread and mixed with the mainstream flow more, causing a reduction in the film cooling effectiveness.

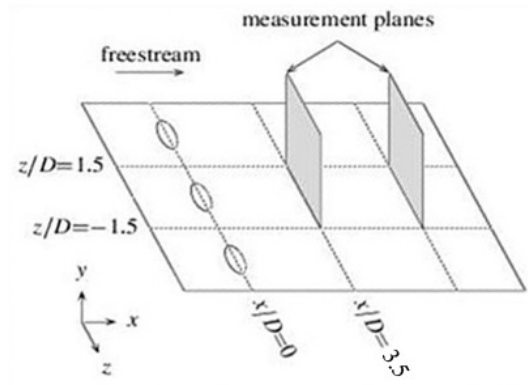
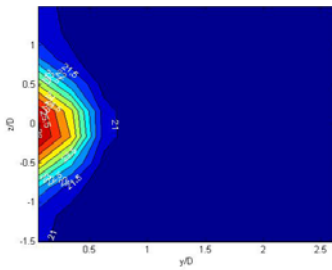


Figure 40: Cold wire temperature plane



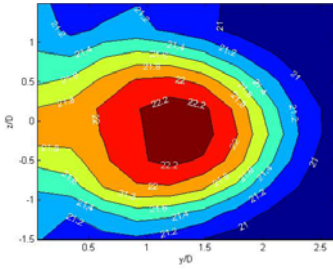


Figure 50: B=1.5 at x=3.5D

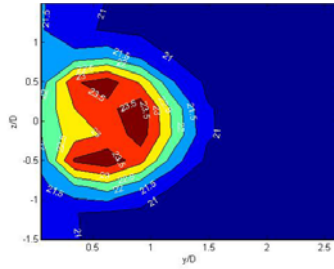


Figure 51: B=1.5 at x=7D

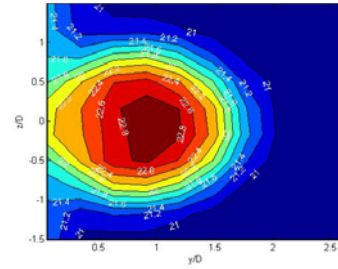


Figure 52: B=1.5 at x=14D

Therefore, for continuous film cooling, the best blowing ratio was $B=0.25$ because it maintained a high film cooling effectiveness throughout the length of the test surface with minimal mass flow. This is further demonstrated in Figures 53 and 54 which show the centerline ($z/D=0$) and spanwise averaged film cooling effectiveness respectively for the various blowing ratios.

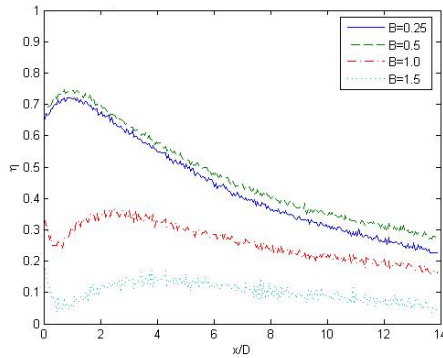


Figure 53: Centerline film cooling effectiveness

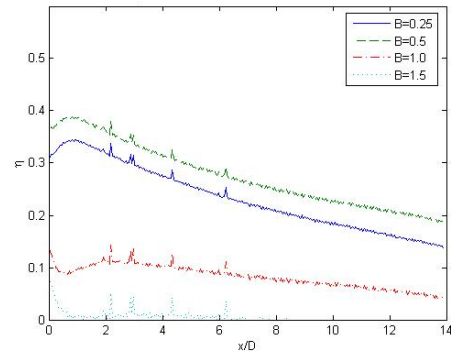


Figure 54: Spanwise average film cooling effectiveness

These film cooling effectiveness results agreed with similar studies in the literature. The results for the blowing ratios of $B=0.25$, 0.5 , and 1.0 matched the results of Sinha *et al.* (1991), the cases of $B=0.5$, 1.0 , and 1.5 matched the results of Gritsch *et al.* (1998), and the $B=0.5$ and 1.0 cases matched the results of Burd and Simon (1998).

Continuous Film Cooling Results – Stanton Numbers

In order to determine the effects of an unheated starting length on the experiments, the Stanton number ratios were determined and compared between the unheated and heated cases.

The Stanton number ratio is a measure of heat transfer between the surface and the mixed mean temperature of the adjacent flow. A high Stanton number indicates high heat transfer, which is generally undesirable when trying to protect the surface, although the undesirable affect can be mitigated by high film cooling effectiveness. Directly downstream of the film cooling holes the jet protected the surface, as shown through the film cooling effectiveness plots. However, there will still be heat transfer between the jet and the surface due to the difference in temperatures. Additionally, there may be an increase in the heat transfer coefficient due to the turbulence and mixing caused by the film cooling jets. In order to determine the effects of both the film cooling effectiveness and Stanton number ratios, the heat flux ratio was also calculated.

Contours of the Stanton number ratio are shown in Figures 55-62. A few features are clear in these figures and show how the film cooling flow enhances the heat transfer rate. Immediately downstream of the film cooling holes, at x/D between 0 and 1.0, there were small regions of high St_f/St_o in all cases at $z/D=\pm 0.5$ around each hole. These regions were believed to be caused by the horseshoe vortex which forms when the main flow boundary layer wraps around the film cooling jet. Another feature was the pair of high St_f/St_o lines which were symmetric about the centerline of each hole and extend downstream along the surface. These were believed to be caused by the kidney vortices associated with the film cooling jets. Between the high St_f/St_o lines, in the region directly downstream of the center of each hole, St_f/St_o was relatively low. Mayhew *et al.* (2002) also observed these lines of high St_f/St_o and called them “fork tines.” Mayhew *et al.* (2002) used a heated wall upstream of their film cooling holes, and suggested that since the fork tine patterns had not been reported in earlier studies with unheated starting regions, that they might result from differences in the upstream boundary condition. In the present study, however, the tines were apparent in cases with both an unheated starting length

and a heated starting length. Mayhew *et al.* (2002) used liquid crystals to visualize and quantify the full temperature field on their test surface. The full temperature field was similarly available in the present study through IR imaging. Perhaps the tines were more apparent in the present study and in Mayhew *et al.* (2002) because of the availability of the full surface temperature field. The limited spatial resolution provided by thermocouple arrays in earlier studies simply did not make the fork tine patterns so obvious.

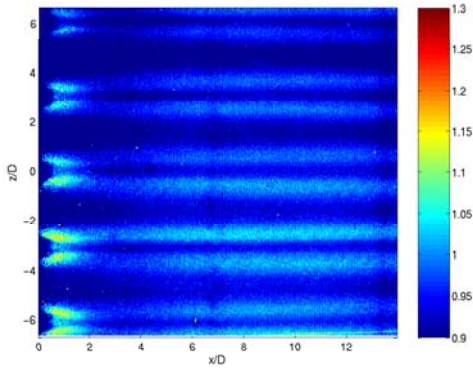


Figure 55: St_f/St_0 at $B=0.25$ with unheated starting length

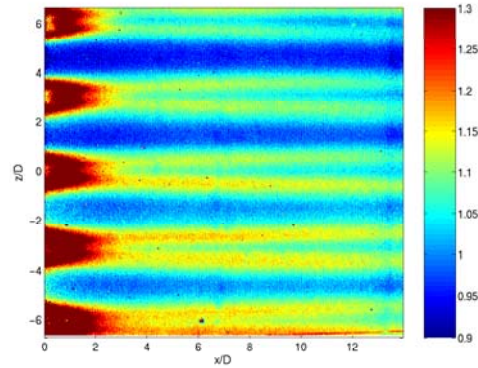


Figure 56: St_f/St_0 at $B=0.25$ with heated starting length

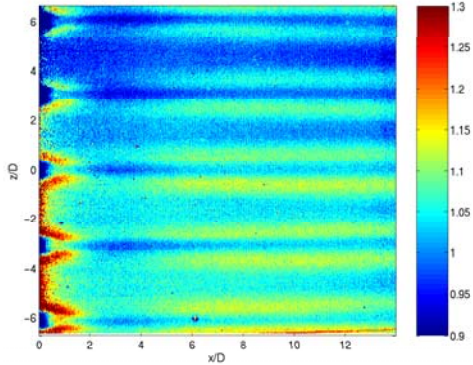


Figure 57: St_f/St_0 at $B=0.5$ with unheated starting length

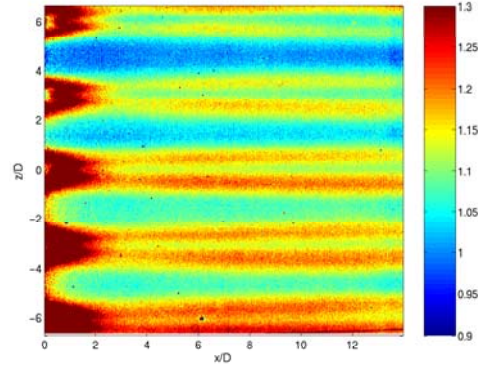
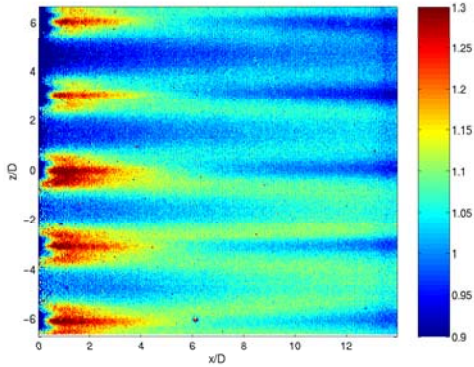
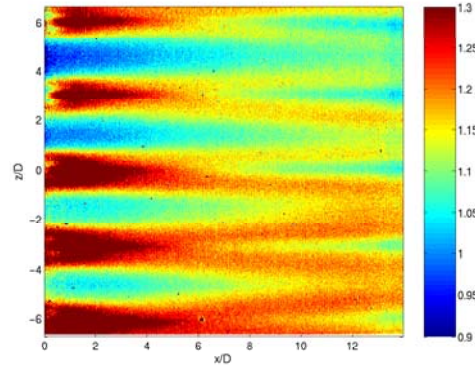
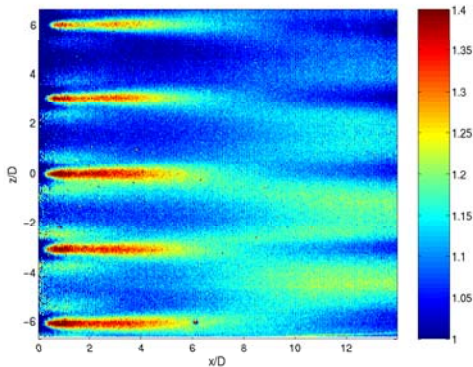
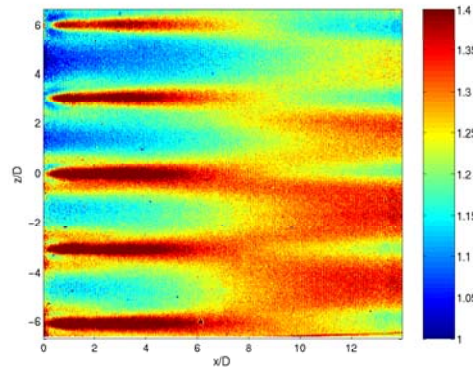


Figure 58: St_f/St_0 at $B=0.5$ with heated starting length

Figure 59: St_f/St_0 at $B=1.0$ with unheated starting lengthFigure 60: St_f/St_0 at $B=1.0$ with heated starting lengthFigure 61: St_f/St_0 at $B=1.5$ with unheated starting lengthFigure 62: St_f/St_0 at $B=1.5$ with heated starting length

For the geometry investigated, the effect of an unheated starting length was most pronounced immediately downstream of the cooling holes. Near the holes, Stanton number ratios were as much as 40% higher for the cases with a heated starting length, particularly at the lower blowing ratios. The difference between the heated and unheated starting length cases decreased with downstream distance from the cooling holes, but differences persisted even 12 diameters downstream of the holes, where Stanton number ratios were still 10 to 15% higher for the heated starting length cases. The flow structure was independent of the wall heating, and caused surface heat transfer patterns which were similar for the heated and unheated starting length cases. The vortices associated with the film cooling jets appeared to produce “fork tined” heat transfer signatures on the wall. Variations in the signatures appeared to be caused by jet

liftoff at higher blowing ratios. More detailed results are presented in Appendix A and referenced from Coulthard *et al.* (2005).

The results thus far have shown that the best case for continuous blowing was $B=0.25$ and that an unheated started length affected the heat transfer results, as shown by the Stanton number ratio. The following tests were run with all the heaters off and with both the upstream and downstream heaters on.

Pulsed Film Cooling Results

Pulsed film cooling is dependent upon three parameters: the frequency, the duty cycle, and the blowing ratio. The frequency is defined as the number of cycles that the jets were pulsed in one second, as shown in Equation 18. The duty cycle is a ratio of the time that the film cooling jet was on to the total time of the cycle, as shown in Equation 19.

$$\text{frequency} = \frac{\# \text{cycles}}{\text{sec}} \quad \text{Equation 18}$$

$$\text{duty cycle} = \frac{\text{jet on time}}{\text{total cycle time}} \quad \text{Equation 19}$$

Pulsed Film Cooling Results – Varying Frequency

Numerous pulsed film cooling cases were run, taking into account a variety of frequencies, duty cycles, and blowing ratios. The varying frequency cases were run at blowing ratios of $B=0.25$, $B=0.5$, $B=1.0$, and $B=1.5$ with a duty cycle of 50% and frequencies of 10 Hz and 20 Hz. Figures 63 and 64 show the film cooling effectiveness contour plots of the $B=0.25$ case at frequencies of 10 Hz and 20 Hz respectively, with Figure 65 relating the centerline film cooling effectiveness of the continuous blowing to the two pulsing cases. Figures 66 and 67 show the Stanton number ratio and heat flux ratio along the centerline at $z/D=0$ for the three cases at $B=0.25$. The negative heat flux ratio values in the steady blowing case resulted when

the film cooling effectiveness was greater than 0.6 (see Equation 14). In practice, the heat flux would not really be negative. The negative values signify that the film cooling is so effective that heat transfer would be negligible. The pulsed cases for the blowing ratio of $B=0.5$ are represented in the same fashion in Figures 68-72 respectively.

Theoretically, pulsing the jet flow at a duty cycle of 50% means that there is half as much mass used for the film cooling process, which could lead to the film cooling effectiveness dropping by 50%. This was demonstrated in the low blowing ratio cases, $B=0.25$ and $B=0.5$, where the pulsed cases had a film cooling effectiveness of approximately half that of the continuous case. Additionally, varying the frequency of the pulsing did not affect the film cooling effectiveness for these low blowing ratios, as shown in Figures 65 and 70. The behavior at $B=0.25$ and $B=0.5$ was essentially the same, so only the $B=0.5$ case was considered further. To further investigate the frequency effect, the case of $B=0.5$ was run again at a frequency of 80 Hz. Figure 70 shows the centerline film cooling effectiveness for the continuous and pulsed cases with three frequencies for $B=0.5$, showing that frequency does not have an effect on the film cooling effectiveness for lower blowing ratios.

Figures 66 and 71 show that although the pulsed cases may have had a lower Stanton number ratio directly downstream of the film cooling holes, the number remained close enough to one that it did not have a significant effect on the heat flux ratio, shown in Figures 67 and 72. The cases with the lower heat flux ratios were the continuous blowing cases. Varying the pulsing frequency did not have a significant effect on the Stanton number ratio at $B=0.25$ and the results of the pulsed cases were similar to the continuous case. Thus, the heat flux ratio was largely dependent upon the film cooling effectiveness. At $B=0.5$, higher pulsing frequency resulted in lower Stanton number ratios directly downstream of the holes. Additional testing is

needed to understand why the Stanton number ratios decreased with higher frequency. Beyond $x=4D$ the ratios from all cases converged to approximately one, which showed that pulsing usually only affected the Stanton number ratio directly downstream of the holes. Although the Stanton number ratios were better for the pulsed cases when compared to the continuous case, the results remained close to one, forcing the heat flux ratio to once again be more dependent upon the film cooling effectiveness. Therefore, pulsed film cooling is not preferred for low blowing ratios with a duty cycle of 50%.

The temperatures of the flow were measured via cold wire at a location $x=3.5D$ downstream of the film cooling holes, in the same location as the temperature fields taken for the continuous cases. At each location in the measurement plane, 2^{17} (131,072) data points were acquired from the cold wire at a 10 kHz sampling rate. At this rate, data were recorded for hundreds of pulsing cycles. The data were then separated based on phase within the pulsing cycle. The data were analyzed at enough phases within the cycle to clearly illustrate the changing behavior of the jet during the cycle. Twenty-four phases separated by 15° was sufficient. The data from each phase angle were averaged to create twenty-four plots of temperature for the different phases in the pulsing cycle. These plots were used as frames to create movie files. The temperature movies were used to visually see the jet pulsing out of the holes and how well it protected the surface. Four frames were taken from these movies to assist in explaining the pulsed results; frames 3, 9, 15, and 21, which represent 45° , 135° , 225° , and 315° in the cycle respectively. Figure 73 shows these frames for the blowing ratio of $B=0.5$ at a frequency of 10 Hz, and Figure 74 shows them for a frequency of 20 Hz. There was minimal difference between the two sets of frames, thus showing that the effects of varying frequency are minimal.

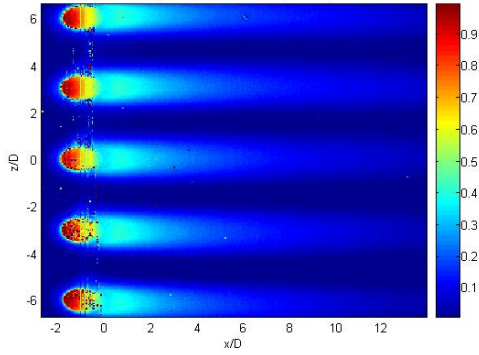


Figure 63: Film cooling effectiveness contour plot for $F=10$ $DC=0.5$ $B=0.25$

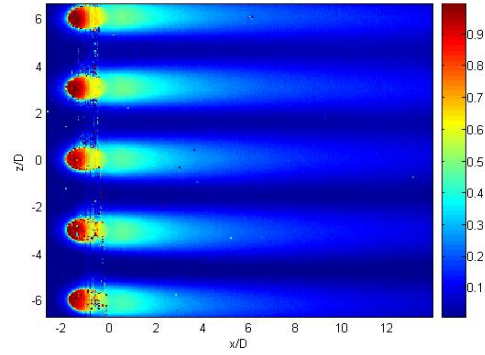


Figure 64: Film cooling effectiveness contour plot for $F=20$ $DC=0.5$ $B=0.25$

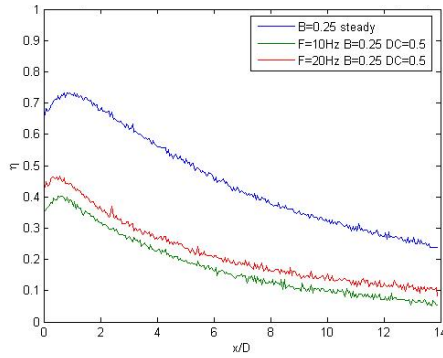


Figure 65: Centerline film cooling effectiveness plot for $B=0.25$

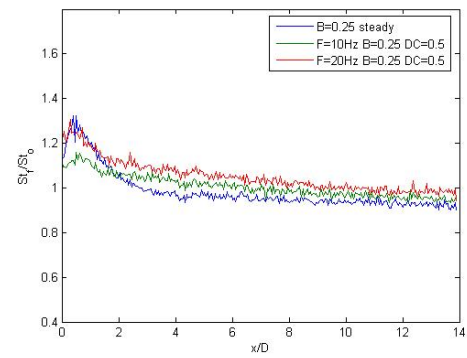


Figure 66: Centerline Stanton number ratio plot for $B=0.25$

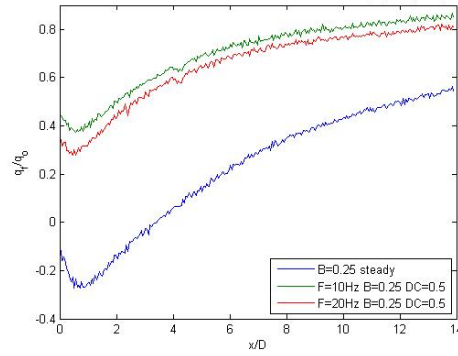


Figure 67: Centerline heat flux ratio for $B=0.25$

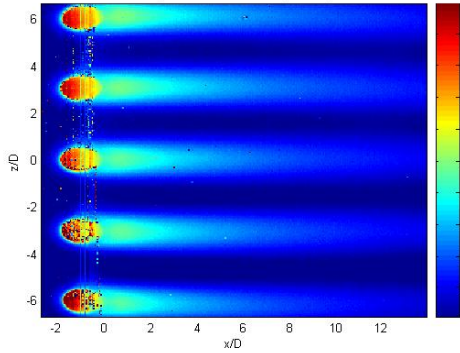


Figure 68: Film cooling effectiveness contour plot for $F=10$ $DC=0.5$ $B=0.5$

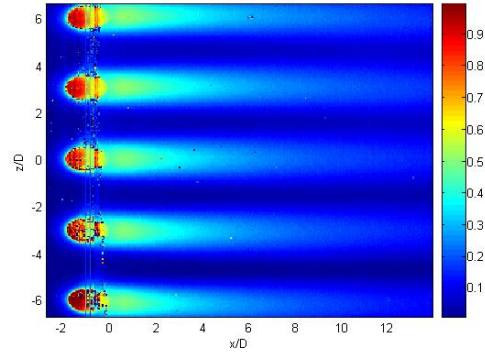


Figure 69: Film cooling effectiveness contour plot for $F=20$ $DC=0.5$ $B=0.5$

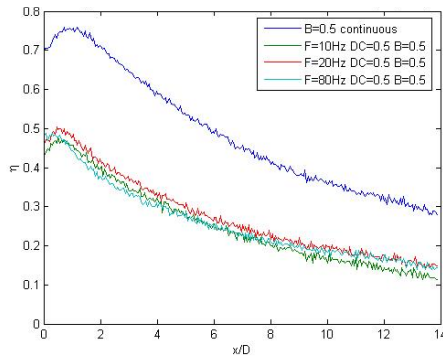


Figure 70: Centerline film cooling effectiveness plot for $B=0.5$

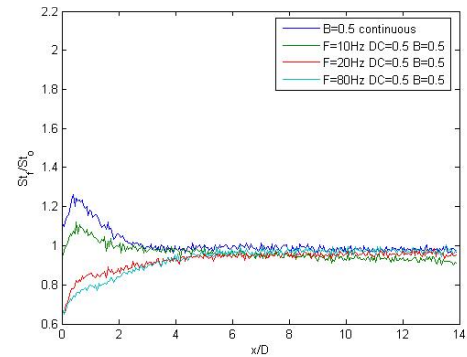


Figure 71: Centerline Stanton number ratio plot for $B=0.5$

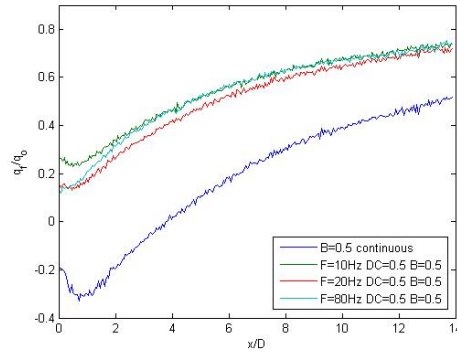


Figure 72: Centerline heat flux ratio for $B=0.5$

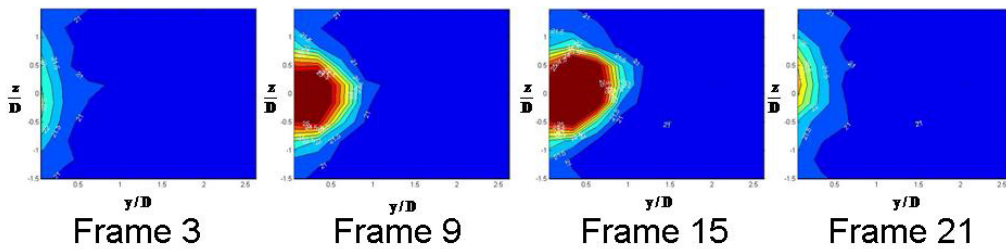


Figure 73: Four frames of 24 frame cycle to show temperature profile for $F=10$ $DC=0.5$ $B=0.5$ at $x=3.5D$

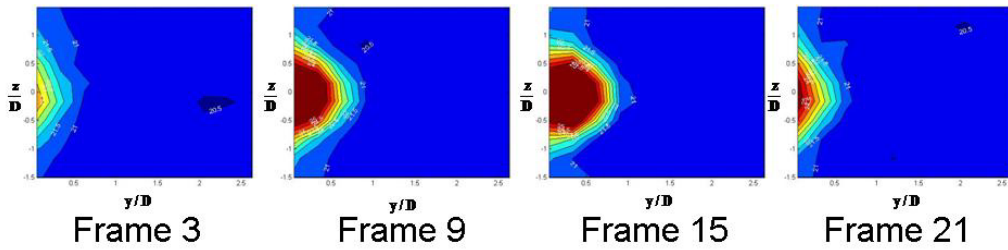


Figure 74: Four frames of 24 frame cycle to show temperature profile for $F=20$ $DC=0.5$ $B=0.5$ at $x=3.5D$

Figures 75 and 76 show the film cooling effectiveness contour plots of the $B=1.0$ case at frequencies of 10 Hz and 20 Hz respectively, with Figure 77 relating the centerline film cooling effectiveness of the continuous blowing case to the two pulsing cases. Figures 78 and 79 show the Stanton number ratio and heat flux ratio along the centerline at $z/D=0$ for the three cases at $B=1.0$. The pulsed cases for the blowing ratio of $B=1.5$ are represented in the same fashion in Figures 80-83 respectively.

Figure 77 shows that pulsing with $B=1.0$ at 10 Hz reduced the film cooling effectiveness by approximately one half due to the 50% reduction in mass flow, similar to the results at $B=0.25$ and $B=0.5$ shown above. However, an increase in the frequency to 20 Hz actually increased the film cooling effectiveness to above the continuous case directly downstream of the film cooling holes, and agreed within the experimental uncertainty with the continuous case further downstream on the test plate. The high velocity of the jet flow was mitigated by the increase in pulsing frequency, meaning that an increased frequency reduces the momentum of the jet. Thus, the jet flow did not experience as much lift off, and by remaining closer to the surface, the increased frequency case caused an increase in film cooling effectiveness. Figures 84 and 85 are of the same four frames as shown above for the $B=0.5$ pulsing cases, but with $B=1.0$ and pulsing frequencies of 10 Hz and 20 Hz respectively. Comparing Figures 84 and 85

to Figure 47 for the continuous $B=1.0$ case, it is apparent that the frequency of 20 Hz allowed the jet to remain closer to the surface for longer periods of time, thus increasing the film cooling effectiveness for that case. The increased frequency also increased the Stanton number ratio significantly directly downstream of the film cooling hole, reaching as high as two. This caused the heat flux ratio to be affected by both the film cooling effectiveness and Stanton number ratio, and it was the highest for the frequency of 20 Hz case. This overall result shows that pulsing was not beneficial for this case.

The momentum in the jets for the $B=1.5$ cases was too high to be reduced by an increase in pulsing frequency. Figure 82 shows that that pulsed cases had approximately the same film cooling effectiveness directly downstream of the film cooling holes. Yet further downstream the effectiveness of the pulsed cases was significantly lower. Surprisingly, the 10 Hz frequency case had a higher film cooling effectiveness than that of the 20 Hz case, which was opposite of the results for $B=1.0$. Therefore, the blowing ratio of $B=1.5$ may have produced jet velocities that were too high for reduction in lift off through either frequency or duty cycle variation. The Stanton number ratio was lower for the higher pulsing frequencies, causing the overall heat flux ratio to be the smallest at the frequency of 20 Hz case. Although pulsing helped improve the heat flux ratio at $B=1.5$, the heat flux ratio was still much higher and the film cooling effectiveness much lower than at the lower blowing ratio cases. Therefore, the case of $B=1.5$ was not explored further.

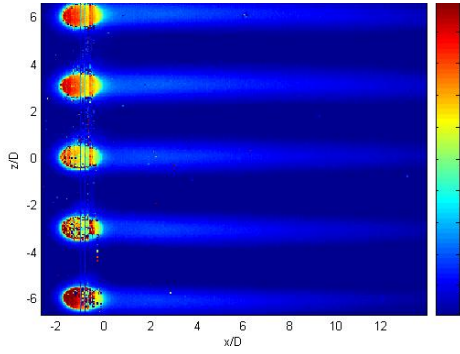


Figure 75: Film cooling effectiveness contour plot for $F=10$ $DC=0.5$ $B=1.0$

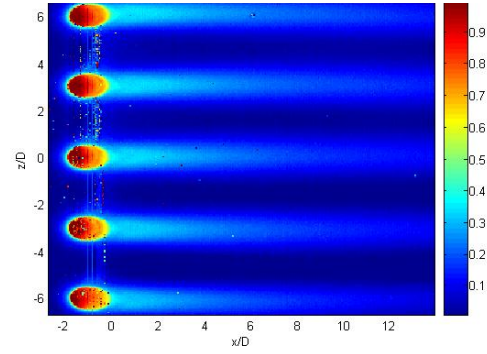


Figure 76: Film cooling effectiveness contour plot for $F=20$ $DC=0.5$ $B=1.0$

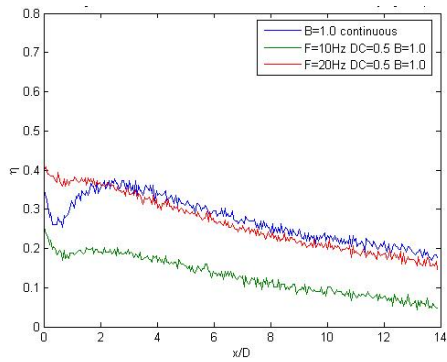


Figure 77: Centerline film cooling effectiveness plot for $B=1.0$

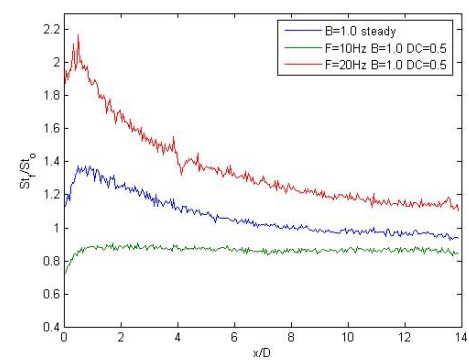


Figure 78: Centerline Stanton number ratio plot for $B=1.0$

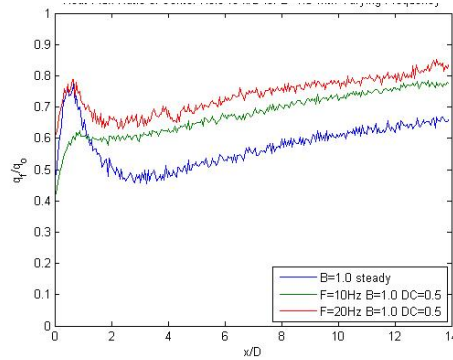


Figure 79: Centerline heat flux ratio plot for $B=1.0$

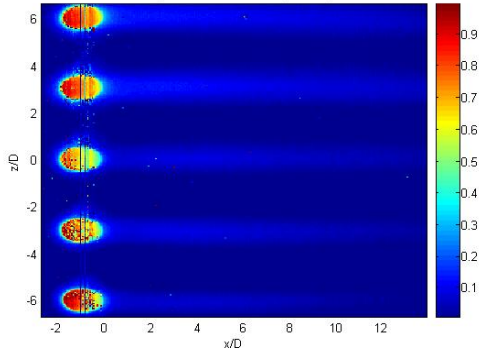


Figure 80: Film cooling effectiveness contour plot for $F=10$ $DC=0.5$ $B=1.5$

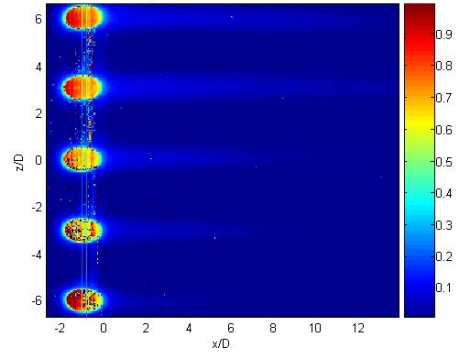


Figure 81: Film cooling effectiveness contour plot for $F=20$ $DC=0.5$ $B=1.5$

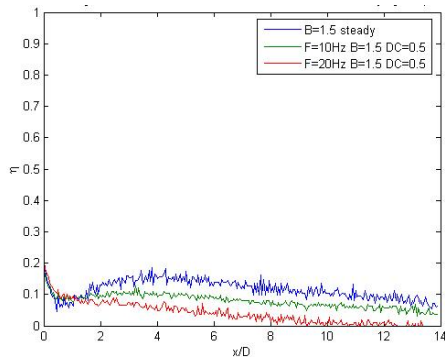


Figure 82: Centerline film cooling effectiveness plot for $B=1.5$

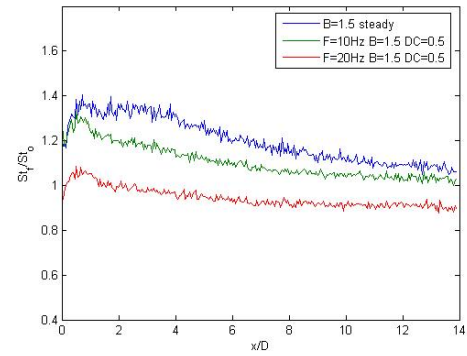


Figure 83: Centerline Stanton number ratio plot for $B=1.5$

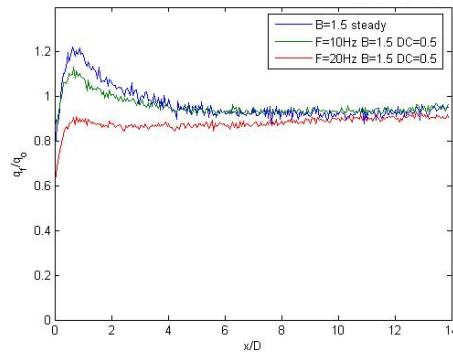


Figure 84: Centerline heat flux ratio plot for $B=1.5$

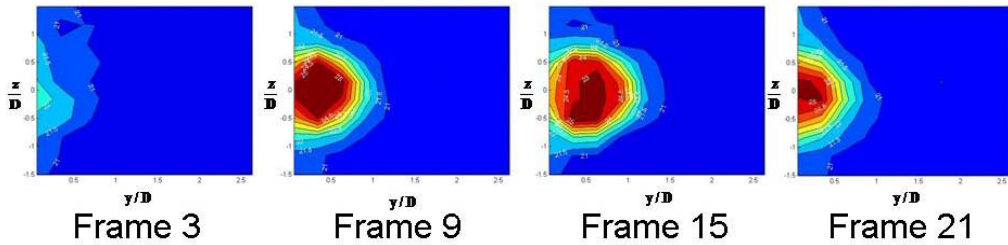


Figure 85: Four frames of 24 frame cycle to show temperature profile for $F=10$ $DC=0.5$ $B=1.0$ at $x=3.5D$

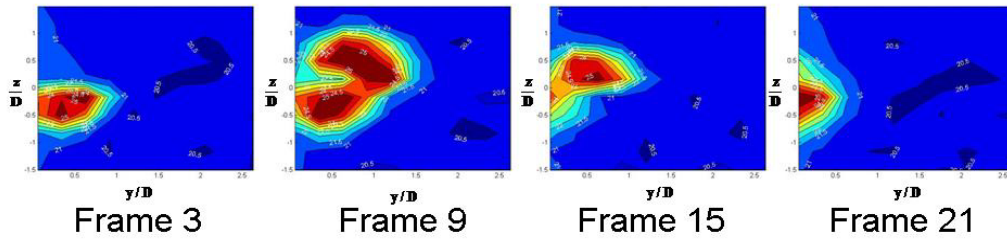


Figure 86: Four frames of 24 frame cycle to show temperature profile for $F=20$ $DC=0.5$ $B=1.0$ at $x=3.5D$

Pulsed Film Cooling Results – Varying Duty Cycle

The next tests were of varying duty cycle with blowing ratios of $B=0.5$ and $B=1.0$. Two additional duty cycles were explored, $DC=0.25$ and $DC=0.75$, with a constant frequency of 20 Hz. The $DC=0.5$ case was discussed previously. Figures 87 and 88 show the film cooling effectiveness contour plots of the $B=0.5$ case at a frequency of 20 Hz and duty cycles of $DC=0.25$ and $DC=0.75$ respectively, with Figure 89 relating the centerline film cooling effectiveness of the continuous blowing case to the three pulsing cases ($DC=0.25, 0.5, 0.75$). Figures 90 and 91 present the Stanton number ratio and heat flux ratio along the centerline at $z/D=0$ for the four cases at $B=0.5$. The pulsed cases for the blowing ratio of $B=1.0$ are presented in the same fashion in Figures 92-96 respectively.

Continuous film cooling can be viewed as pulsing the film cooling jet at a duty cycle of one; the jet is always on. Thus, as the duty cycle decreases, the mass flow used for film cooling also decreases. Theoretically, this would proportionally affect the film cooling effectiveness. This was the case for $B=0.5$, when the duty cycles varied from 0.25 to 1.00, the film cooling effectiveness changed proportionally. The Stanton number ratio improved for the pulsing cases, as shown in Figure 90, however the value remained near one. Therefore, the heat flux ratio was lowest for the continuous case since it was mostly dependent upon the film cooling effectiveness. Figures 97 and 98 show the four frame phase temperature contour plots for duty cycles of

DC=0.25 and DC=0.75 respectively, for a frequency of 20 Hz. Figure 73 shows the effects of a duty cycle of DC=0.5. It can be seen through Figure 97 that in a DC=0.25 case the jet was only on 25% of the time, hence only 25% of the mass was being used for film cooling and the surface was left exposed. On the other hand, in Figure 98, the duty cycle of DC=0.75 case showed that using more mass for film cooling allowed the jet flow to protect the surface for a longer period of time as the duty cycle increased. Figure 44 shows the duty cycle of DC=1.0 case; continuous film cooling.

In the $B=1.0$ cases with a frequency of 20 Hz, as the duty cycle decreased from one (continuous blowing), the film cooling effectiveness increased until a certain limit was reached. The reduction in duty cycle limited the velocity of the jet and reduced lift off similar to how the increased frequency did for high blowing ratios. Therefore, as the duty cycle decreased, the velocity and momentum of the jet flow decreased, providing an attached flow to the surface of the plate. This occurred until there was too little mass to effectively protect the plate, as in the case of DC=0.25. This can be seen in Figure 94, where the cases with DC=0.5 and 0.75 had a higher film cooling effectiveness than the continuous case directly downstream of the film cooling holes. Additionally, the case of DC=0.75 had a lower Stanton number ratio, and the combination of improved film cooling effectiveness and Stanton number ratio over the continuous case resulted in it having a lower heat flux ratio, as shown in Figures 95 and 96. Figures 99 and 100 show the four frame phase temperature contour plots for duty cycles of DC=0.25 and DC=0.75 respectively, for a frequency of 20 Hz. Figure 86 shows the effects of a duty cycle of DC=0.5 and Figure 47 can be used for a comparison to continuous cooling. These plots show that too low of a duty cycle did not allow enough mass for proper surface protection (DC=0.25), but middle-range duty cycles (DC=0.5, 0.75) decreased jet lift off.

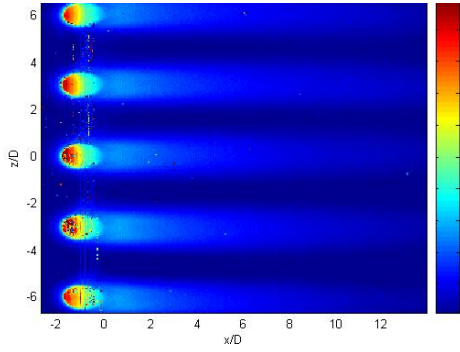


Figure 87: Film cooling effectiveness contour plot for $F=20$ $DC=0.25$ $B=0.5$

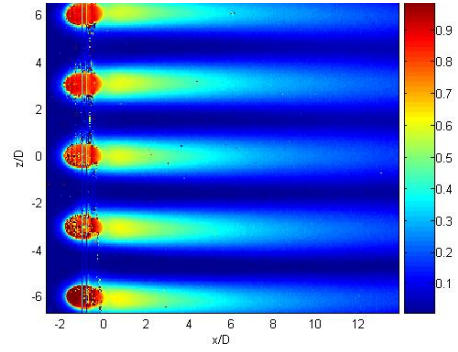


Figure 88: Film cooling effectiveness contour plot for $F=20$ $DC=0.75$ $B=0.5$

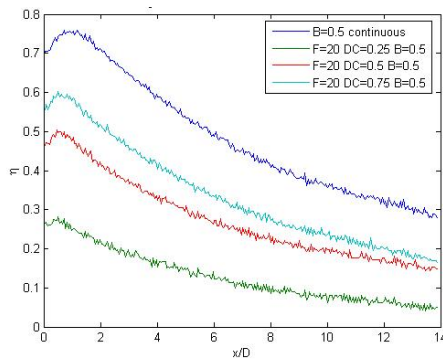


Figure 89: Centerline film cooling effectiveness for $B=0.5$ with varying duty cycle.

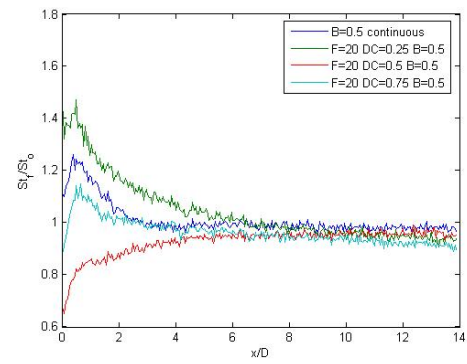


Figure 90: Centerline Stanton number ratio plot for $B=0.5$ with varying duty cycle

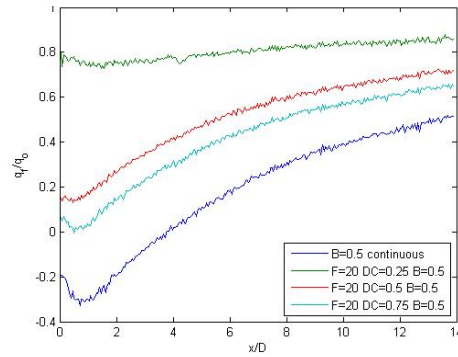


Figure 91: Centerline heat flux ratio for $B=0.5$ with varying duty cycle

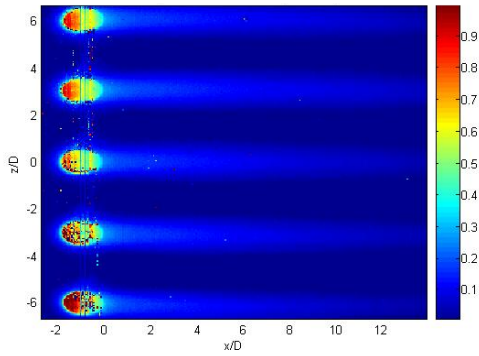


Figure 92: Film cooling effectiveness contour plot for $F=20$ $DC=0.25$ $B=1.0$

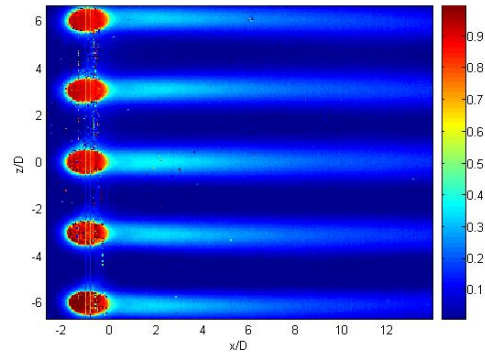


Figure 93: Film cooling effectiveness contour plot for $F=20$ $DC=0.75$ $B=1.0$

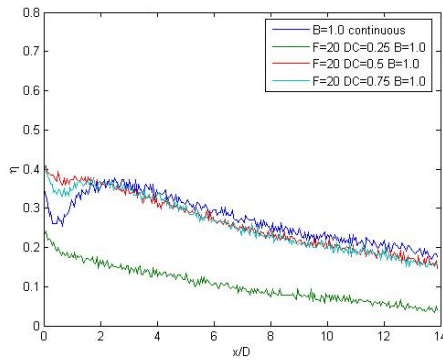


Figure 94: Centerline film cooling effectiveness plot for $B=1.0$ with varying duty cycle

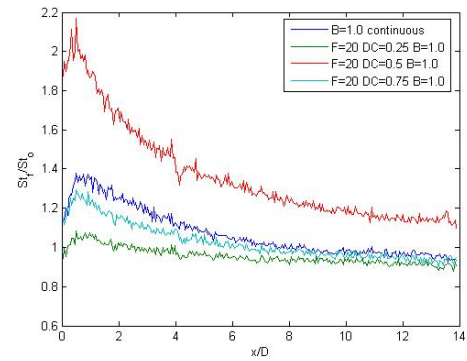


Figure 95: Centerline Stanton number ratio plot for $B=1.0$ with varying duty cycle

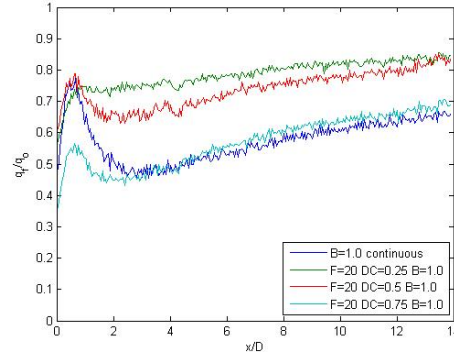


Figure 96: Centerline film cooling effectiveness plot for $B=1.0$ with varying duty cycle

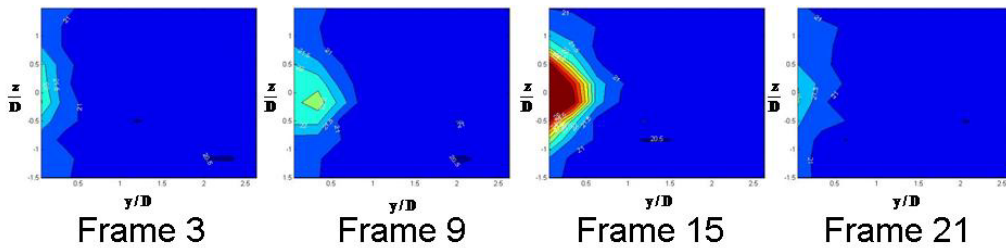


Figure 97: Four frames of 24 frame cycle to show temperature profile for $F=20$ $DC=0.25$ $B=0.50$ at $x=3.5D$

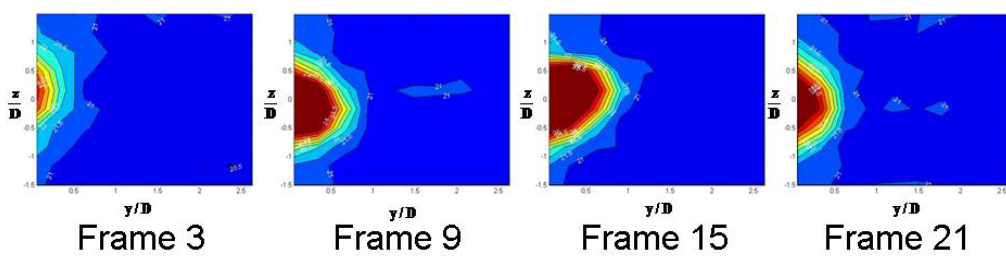


Figure 98: Four frames of 24 frame cycle to show temperature profile for $F=20$ $DC=0.75$ $B=0.5$ at $x=3.5D$

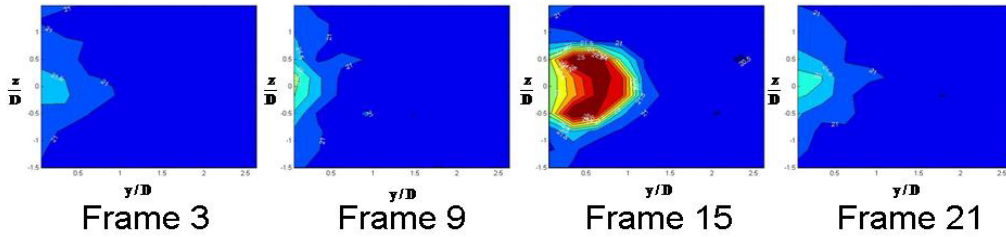


Figure 99: Four frames of 24 frame cycle to show temperature profile for $F=20$ $DC=0.25$ $B=1.0$ at $x=3.5D$

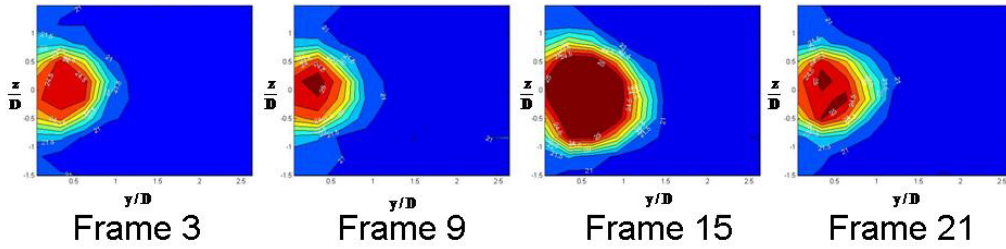


Figure 100: Four frames of 24 frame cycle to show temperature profile for $F=20$ $DC=0.75$ $B=1.0$ at $x=3.5D$

In summary, varying the frequency had minimal effect on the film cooling effectiveness for pulsed cases with $B=0.5$ due to the decrease in mass flow. An increase in frequency resulted in a significant improvement to the film cooling effectiveness with $B=1.0$, however, due to the decrease in jet lift off. Varying the duty cycle affected the film cooling effectiveness proportionally with mass flow for $B=0.5$ cases. Decreasing the duty cycle for the $B=1.0$ cases improved the film cooling effectiveness, Stanton number, and thus heat flux ratio to better than the continuous results by minimizing the effects of jet lift off.

Conclusions

This study showed the effect of blowing ratio, pulsing frequency, and pulsing duty cycle on film cooling effectiveness, and also demonstrated the importance of a heated starting length for thermal boundary layer analysis. For the cases considered, the overall best case was continuous blowing at $B=0.25$ because it had the highest film cooling effectiveness while using the least amount of mass. Pulsed film cooling improved the film cooling effectiveness for higher blowing ratios ($B=1.0$) particularly with increasing frequency and decreasing duty cycles. These parameters reduced jet lift off that was apparent in continuous blowing cases, thus increasing the film cooling effectiveness. However, even with these increases, the film cooling effectiveness was still below the film cooling effectiveness of the $B=0.25$ case with continuous blowing. Therefore, although pulsed film cooling was not superior to continuous cooling for all the cases considered, it was beneficial for some cases, particularly at higher blowing ratios. Additional research is needed in more complex conditions to determine whether, and under what conditions, pulsed film cooling may be beneficial. These other conditions include having more rows of film cooling holes, curvature affects, rotational affects, and high freestream turbulence.

	B=0.125	B=0.25	B=0.5	B=1.0	B=1.5
No Blowing					
Continuous Blowing	Best only directly downstream	OVERALL BEST CASE	2nd best case overall	Worse than some pulsing cases	Worse than some pulsing cases
Heating	Showed importance of a heated starting length.				
Pulsing - Varying Frequency					
F=10Hz DC=0.5		Improved St_f/St_o	Improved St_f/St_o	Improved q_f/q_o directly downstream	Improved q_f/q_o
F=20Hz DC=0.5		Improved St_f/St_o	Improved St_f/St_o	Improved η	Improved q_f/q_o
F=80Hz DC=0.5			Improved St_f/St_o		
Pulsing - Varying Duty Cycle					
F=20Hz DC=0.25				Improved St_f/St_o	
F=20Hz DC=0.75			Improved St_f/St_o	BEST PULSING CASE	

Table 2: Results.

Bibliography

Bons, J.P., MacArthur, C.D., and Rivir, R.B., 1994, "The Effect of High Freestream Turbulence of Film Cooling Effectiveness," ASME Paper 94-GT-51.

Bons, J.P., Rivir, R.B., MacArthur, C.D., Pestian, D.J., 1996, "The Effect of Unsteadiness on Film Cooling Effectiveness," WLTR-96-2096.

Bons, J.P., Sondergaard, R., and Rivir, R.B., 2002, "The Fluid Dynamics of LPT Blade Separation Control Using Pulsed Jets," ASME Paper 2001-GT-190.

Burd, S., Kasezeta, R.W., and Simon, T.W., 1998, "Measurements in Film Cooling Flows: Hole L/D and Turbulence Intensity Effects," *Journal of Turbomachinery*, Vol. 120, pp. 791-798.

Burd, S. and Simon, T.W., 2000, "Effects of Hole Length, Supply Plenum Geometry, and Freestream Turbulence on Film Cooling Performance," NASA, CR-210336.

Çengel, Y.A. and Boles, M.A., 2002, "Thermodynamics: An Engineering Approach," McGraw Hill, Ed. 4, p. 471.

Coulthard, S.M., Volino, R.J., Flack, K.A., "Effect of Unheated Starting Lengths on Film Cooling Experiments," ASME Paper HT2005-72392, submitted for the ASME Summer Heat Transfer Conference, San Francisco, California, July 2005, and to the ASME Journal of Turbomachinery.

Crawford, M.E. and Kayes, W.M., 1976, "STAN5 * A Program for Numerical Computation of Two-Dimensional Internal and External Boundary Layer Flows," NASA CR 2742.

Ekkad, S.V., Ou, S., and Rivir, R.B., 2004, "Effect of Jet Pulsation and Duty Cycle on Film Cooling from a Single Jet on a Leading Edge Model," Proceedings of IMECE04 ASME International Mechanical Engineering Congress and Exposition November 13-20, 2004, Anaheim, California USA, ASME paper number IMECE2004-60466.

Foster, N.W. and Lampard, D., 1980, "The Flow and Film Cooling Effectiveness Following Injection Through a Row of Holes," *J. Engineering for Power*, Vol. 102, pp. 584-588.

Gritsch, M., Schulz, A., and Wittig, S., 1998, "Adiabatic Wall Effectiveness Measurements of Film-Cooling Holes With Expanded Exits," *Journal of Turbomachinery*, Vol. 120, pp. 549-556.

Jung, I.S., Lee, J.S., and Ligrani, P.M., 2002, "Effects of Bulk Flow Pulsations on Film Cooling With Compound Angle Holes: Heat Transfer Coefficient Ratio and Heat Flux Ratio," *Journal of Turbomachinery*, Vol. 124, pp. 142-151.

Kelly, G.B. and Bogard, D.G., 2003, "An Investigation of the Heat Transfer for Full Coverage Film Cooling," ASME Paper GT2003-38716.

Lakshminarayana, B., 1996, "Fluid Dynamics and Heat Transfer of Turbomachinery," John Wiley & Sons, Inc, pp. 656-683.

LeBrocq, P.V., Launder, B.E., and Priddin, C.H., 1973, "Discrete Hole Injection as a Means of Transpiration Cooling: An Experimental Study," *Proc. Inst. Mech. Eng.*, Vol. 187, pp. 149-157.

Ligrani, P.M., Gong, R., Cuthrell, J.M., and Lee, J.S., 1996, "Bulk Flow Pulsations and Film Cooling: Part 2, Flow Structure and Film Effectiveness," *International Journal of Heat and Mass Transfer*, Vol. 39, No. 11, pp. 2283-2292.

Mayhew, J.E., Baughn, J.W., and Byerley, A.R., 2002, "The Effect of Freestream Turbulence on Film Cooling Heat Transfer Coefficient," ASME Paper GT-2002-30713.

Munson, B.R., Young, D.F., and Okiishi, T.H., 2002, "Fundamentals of Fluid Mechanics," John Wiley & Sons, Inc, Ed. 4, p. 404.

Pratt and Whitney, 2002, Cutaway - PW4000-112" Engine, 20 Jan. 2004, <http://www.pw.utc.com/presskit/images/pw4000112_cutaway_high.jpg>.

Sinha, A.K., Bogard, D.G., and Crawford, M.E., 1991, "Film-Cooling Effectiveness Downstream of a Single Row of Holes With Variable Density Ratio," *Journal of Turbomachinery*, Vol. 113, pp. 442-449.

Sizov, M., 2003, "Numerical Optimization of the Air Film Cooling," The Scientific Computing Group, 20 Jan. 2004, <<http://www.win.tue.nl/scg/research/phdprojects/sizov.html>>.

VKI Lecture Series, 1982, "Film Cooling and Turbine Blade Heat Transfer," Vols. 1 and 2, VKI LS 82-02.

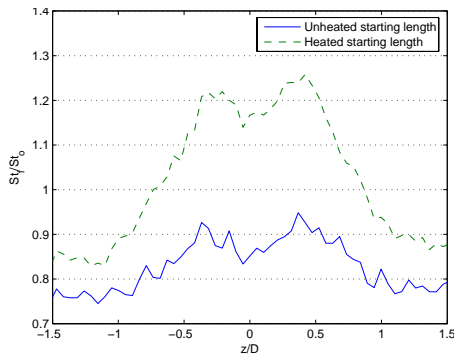
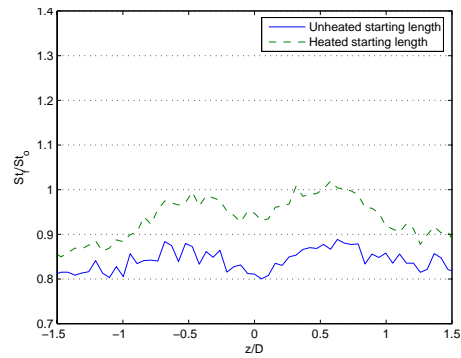
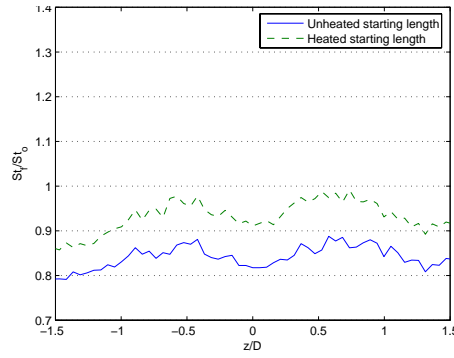
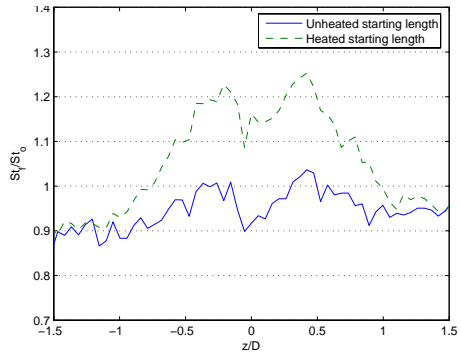
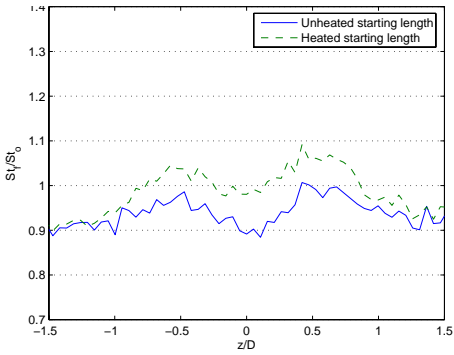
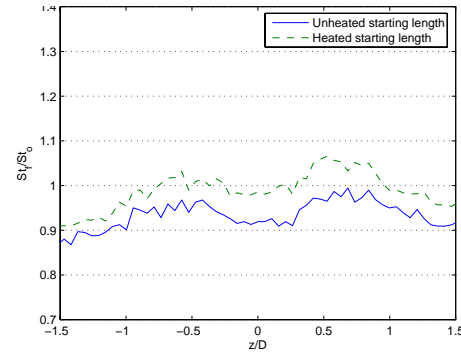
Appendix A

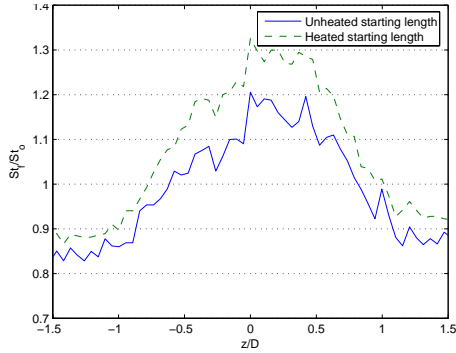
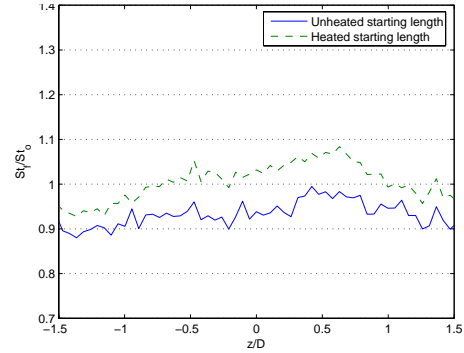
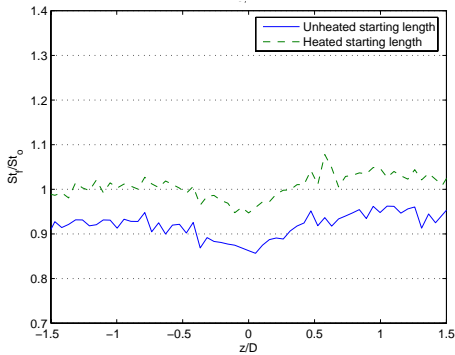
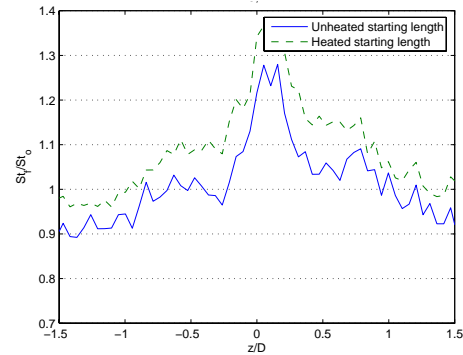
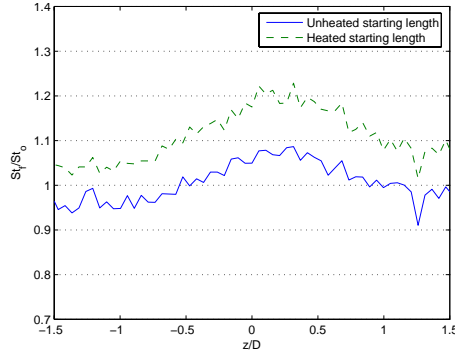
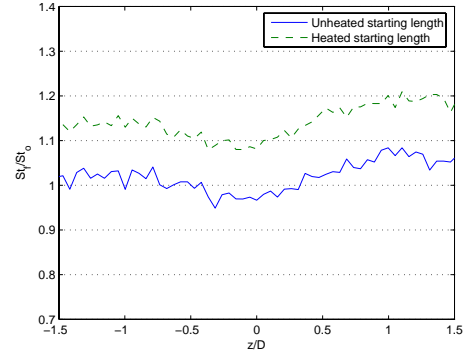
Details of the Unheated Starting Length

In order to determine the effects of an unheated starting length on the experiments, the Stanton number ratios were determined and compared between the unheated and heated cases. Contours of the Stanton number ratio are shown in Figures 55-62, which present the effects of kidney vortices associated with the film cooling jets.

A heated starting length generally increases the St_f/St_o ratio, as shown in Figures 55-62. At each blowing ratio, the St_f/St_o patterns were very similar in the unheated (Figures 55, 57, 59, 61) and heated (Figures 56, 58, 60, 62) cases, but the features were more distinct due to the higher St_f/St_o values with the heated starting length. At the lower blowing ratios, this was particularly apparent downstream of each hole in the region $0 < x/D < 2$. This was illustrated more quantitatively in Figures A-1 and A-4, which showed spanwise profiles of St_f/St_o for the $B=0.25$ and $B=0.5$ cases at $x/D=1$. The St_f/St_o ratio was between 30% and 40% greater in the heated starting length cases. Kelly and Bogard (2003) saw similar results. They noted that the film cooling jet forces the start of a new thermal boundary layer, regardless of the upstream boundary condition. Hence, the St_f values for the heated and unheated starting length cases were about the same. Without film cooling, however, St_o in the present study was about 35% higher with an unheated starting length. This helps explain the high St_f/St_o values. The fork tines were apparent in Figures A-1 and A-4 in both the heated and unheated starting length cases as double peaks in the St_f/St_o ratios at $z/D=\pm 0.3$. The tines extended directly downstream in the $B=0.25$ and $B=0.5$ cases. Figures A-2 and A-3 showed spanwise profiles of St_f/St_o at $x/D=6$ and 12 respectively for the $B=0.25$ case. The difference between the heated and unheated starting length cases was not as strong as was observed upstream, but the St_f/St_o ratio was still about 15% higher for the

unheated case. The spacing of the tines increased to $z/D=\pm 0.5$ at $x/D=6$, and remained about the same at $x/D=12$. Figures A-5 and A-6 show similar results at $x/D=6$ and 12 for the $B=0.5$ case. With $B=0.5$, St_f/St_0 was about 10% higher in the unheated starting length case at the downstream locations. The tine spacings were about the same for the $B=0.25$ and $B=0.5$ cases. Mayhew *et al.* (2002) showed that the tine spacing remained essentially constant for their $B=0.5$ case. They provide documentation to $x/D=27$.

Figure A-1: St_f/St_0 at $B=0.25$ and $x/D=1$ Figure A-2: St_f/St_0 at $B=0.25$ and $x/D=6$ Figure A-3: St_f/St_0 at $B=0.25$ and $x/D=12$ Figure A-4: St_f/St_0 at $B=0.5$ and $x/D=1$ Figure A-5: St_f/St_0 at $B=0.5$ and $x/D=6$ Figure A-6: St_f/St_0 at $B=0.5$ and $x/D=12$

Figure A-7: St_f/St_0 at $B=1.0$ and $x/D=1$ Figure A-8: St_f/St_0 at $B=1.0$ and $x/D=6$ Figure A-9: St_f/St_0 at $B=1.0$ and $x/D=12$ Figure A-10: St_f/St_0 at $B=1.5$ and $x/D=1$ Figure A-11: St_f/St_0 at $B=1.5$ and $x/D=6$ Figure A-12: St_f/St_0 at $B=1.5$ and $x/D=12$

As the blowing ratio increases, the fork tines spread outward in the spanwise direction, causing the tines of one hole to interfere with and merge with those of the adjacent film cooling holes. This merging occurred at x/D of about 13 in the $B=1.0$ case (Figures 59, 60) and at x/D of about 10 in the $B=1.5$ case (Figures 61, 62). Mayhew *et al.* (2002) observed the same merging at these blowing ratios. They noted that the merging results in high heat transfer coefficients at the

spanwise positions midway between the film cooling holes, and that this could be particularly detrimental since the film cooling effectiveness is lowest at these spanwise positions. Another difference between the high and low blowing ratio cases was a narrow band of high St_f/St_o in the region between the tines, directly downstream of the center of the film cooling holes. This band extended to about $x/D=6$ with $B=1.0$ and to $x/D=7$ with $B=1.5$. The end of the band corresponded to the position where the fork tines began to spread. The increased blowing ratio lengthened the distance of high heat transfer directly downstream of the holes, and increased the slope of the fork tines during separation. Thus the tines separated at a further streamwise distance, yet merged at a closer streamwise distance. The behavior described above was true for both the unheated and heated starting length cases.

Figures A-7-A-9 show spanwise profiles of St_f/St_o for a blowing ratio of $B=1.0$. These figures also show that the difference between the unheated and heated starting length cases was not as great as it was for lower blowing ratios, particularly at $x/D=1$, where St_f/St_o was only about 15% higher for the heated starting length case. At $x/D=6$ and 12, the difference was about 10%. The region directly behind the film cooling holes did not exhibit the fork tines, as shown in Figure A-7. By $x/D=6$, the fork tines had begun to form, but they were not as clear as at the lower blowing ratios. By $x/D=12$ the tines had joined with the adjacent tines, with peaks at $z/D=\pm 1$. Figures A-10-A-12 show similar behavior at a blowing ratio of $B=1.5$. At $x/D=1$ and $x/D=6$ the fork tines were absent, with a region of high heat transfer downstream of the holes centered at $z/D=0$. By $x/D=12$, heat transfer was lowest at $z/D=0$ and highest at $z/D=\pm 1.5$, where the tines had merged. The difference in the St_f/St_o ratio between the heated and unheated starting length cases was about 15% at $B=1.5$.

Flow measurements can help explain the heat transfer behavior described above. In the $B=0.25$ and $B=0.5$ cases, the film cooling jets remained near the wall, as evidenced by the high film cooling effectiveness of Figures 53-54 and the flow temperature measurements of Figures 41-46. Figures A-13-A-15 show contours of the rms fluctuating temperature in the flow in planes at three streamwise positions for the $B=0.5$ case. These contours along with mean temperature contours (Figures 44-46) indicated that the jet fluid was adjacent to the wall, with the core of the jet located at about $y/D=0.2$. The shape of the fluctuating temperature profiles suggested the kidney shaped vortices which form in the film cooling jet. These vortices within the jet would cause fluid to impinge on the wall at about $z/D=\pm 0.5$, causing the high St_f of the fork tines at these spanwise locations. The relatively calm fluid between the tines resulted in lower heat transfer along the centerline downstream of the film cooling holes.

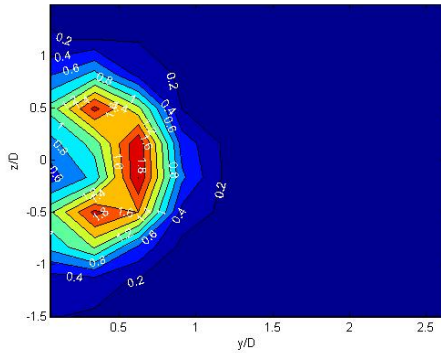


Figure A-13: Temperature Variation for $B=0.5$ at $x/D=3.5$

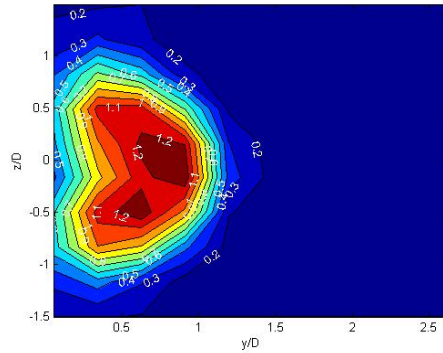


Figure A-14: Temperature Variation for $B=0.5$ at $x/D=7$

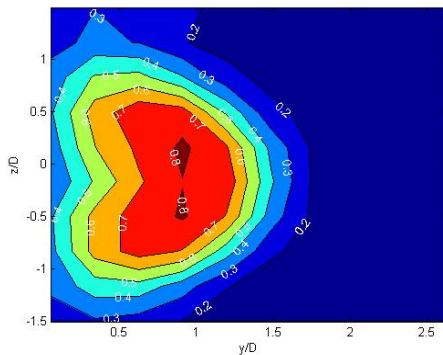


Figure A-15: Temperature Variation for $B=0.5$ at $x/D=14$

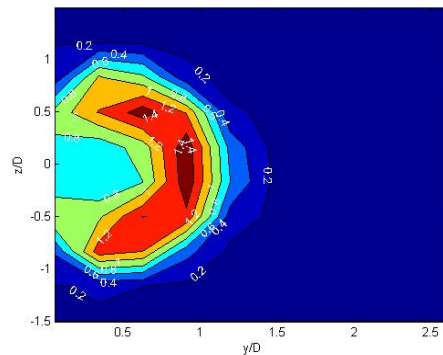


Figure A-16: Temperature Variation for $B=1.0$ at $x/D=3.5$

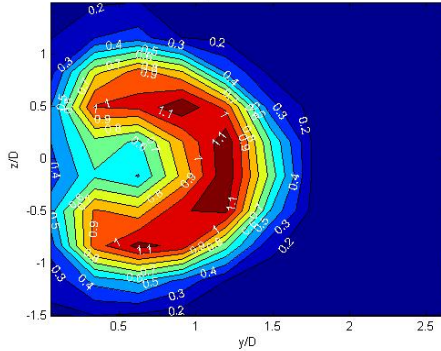


Figure A-17: Temperature Variation for B=1.0
at $x/D=7$

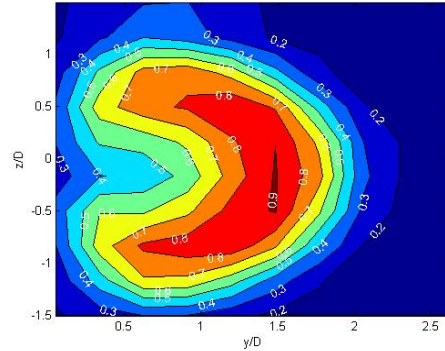


Figure A-18: Temperature Variation for B=1.0
at $x/D=14$

For the $B=1.0$ and $B=1.5$ cases, the film cooling jets lifted off the wall upon exiting the holes. The fluctuating temperature contours of Figures A-16-A-18, along with the corresponding mean temperature contours (Figures 47-49), indicated that the core of the film cooling jet was considerably farther from the wall than in the $B=0.5$ case. This observation was supported by the lower film cooling effectiveness for the higher blowing rate cases in Figures 53 and 54. When the jets lifted off the wall, the interaction with the main flow likely created more turbulence than in the lower blowing rate cases. This may explain the region of high heat transfer coefficient directly downstream of the holes in the $B=1.0$ and $B=1.5$ cases. The jet fluid was apparently too far from the wall to produce the fork tine signature immediately downstream of the holes. At these blowing ratios the jet flow did not reach the test wall until further downstream, at which point the spreading fork tine signature appears.

For the geometry investigated, the effect of an unheated starting length was most pronounced immediately downstream of the cooling holes. Near the holes, Stanton number ratios were as much as 40% higher for the cases with a heated starting length, particularly at the lower blowing ratios. The difference between the heated and unheated starting length cases decreased with downstream distance from the cooling holes, but differences persisted even 12

diameters downstream of the holes, where Stanton number ratios were still 10 to 15% higher for the heated starting length cases. The flow structure was independent of the wall heating, and caused surface heat transfer patterns which were similar for the heated and unheated starting length cases. The vortices associated with the film cooling jets appeared to produce “fork tined” heat transfer signatures on the wall. Variations in the signatures appeared to be caused by jet liftoff at higher blowing ratios.